HOMOGENIZATION AND ELASTIC-PLASTIC TRANSITIONS IN RANDOM AND FGM MICROSTRUCTURES

BY

ANKIT SAHARAN

DISSERTATION

Submitted in partial fulfillment of the requirements
for the degree of Doctor of Philosophy in Mechanical Engineering
in the Graduate College of the
University of Illinois at Urbana-Champaign, 2015

Urbana, Illinois

Doctoral Committee:

Professor Martin Ostoja-Starzewski, Chair & Director of Research
Professor Harry H. Hilton
Professor Huseyin Sehitoglu
Adjunct Professor Seid Koric

Abstract

The research presented here uses homogenization as a tool to estimate the effective properties of heterogeneous materials with varying microstructures. Separation of scales (Micro (d), Meso(δ), Macro (L)), in these microstructures leads to the problem of determination of the Representative Volume Element (RVE) that corresponds to the effective properties of materials. Microstructural randomness is inherent in these materials and hence we study the scaling from Statistical Volume Element (SVE) to RVE. Using Hill condition, the RVE is achieved when the material response becomes independent of the two boundary conditions (kinematic and static boundary condition) setup on the SVE. Elastic responses of 2d microstructures such as two-phase random checkerboard are considered, and RVE of the same is also identified. This technique is consistent with the Hill-Mandel macrohomogenity condition. We propose to homogenize the elastic response of FGM (functionally graded materials) type microstructure in 3d using the same technique. Since the Hill condition is independent of the microstructure, hence it is counter-intuitive that FGM microstructure cannot be easily homogenized using the same approach. The inelastic response of FGM microstructures in 2d and 3d are also studied here. The elastic-plastic transition in multiphase materials is smooth (not sudden), suggesting fractal nature of the evolving plasticity in the material. An attempt is made to calculate the fractal dimension of these evolving plastic grains in the 2d and 3d FGM microstructure. In 3d, this results in massive simulations performed in parallel using commercially available FEM package called ABAQUS. The simulations were carried out using the computational resources available at the National Center for Supercomputing Applications (NCSA). This opens up the possibility of assessing plastic damage in material through fractals. Preliminary experimental study using viscoelastic materials for FGM microstructure is also presented here. Furthermore, we also present the scaling effect under finite mesoscale size quantified in the form of normalized scaling function. We propose to study the effect of this scaling function for the two-phase correlated microstructures of Gaussian type, formulation of which is also presented here. Comparison with existing experimental data shows our numerical model is well in agreement with the experimental data for various volume fractions of the constituent phases.

To my family.

Acknowledgments

This project would not have been possible without the support of many people. Many thanks to my adviser, Prof. Martin Ostoja-Starzewski, who read my numerous revisions and helped make some sense of the confusion. Also thanks to my committee members, Prof. Harry H. Hilton, Prof. Huseyin Sehitoglu, and Dr. Seid Koric, who offered guidance and support.

I would also like to express my gratitude to Dr. Kathy Walsh, postdoctoral research associate at Seitz Materials Research Lab for helping me conduct experiments on my 3D printed FGM samples.

I wish to thank my lab mates, Sohan Kale, Vinesh Nishawala, Jun Zhang, Dansong Zhang for their friendly assistance and many discussions. I would like to thank the support staff in MechSE department, especially Kathy Smith for assisting me in many non-technical matters during the course of my graduate study.

Finally, I express my endless gratitude to my parents, Anil Saharan and Rekha Saharan, and my wife Shweta Saharan, who consistently gave me love, support and motivation.

Table of Contents

List of Tables

List of Figures

Chapter 1

Introduction

1.1 Motivation

Engineering materials involve a wide variety of systems, all of them offering various ways of classification and characterization according to their mode of manufacture; their attributes (like thermal, mechanical, or electrical properties), or their usage [32]. With an ever-increasing need for materials with higher functionality, it has been a known fact that single-phase homogeneous materials have a limited scope of applicability. As such, multi-phase materials have become the preferred materials for current engineering applications. However, estimation of properties of these multi-phase materials in not trivial. Early research resulted in the famous Voigt [56] and Reuss [48] bounds (the well known *'Rule of mixtures'*), and then led to improved Hashin-Shtrikman [17] bounds. However, these bounds are independent of most details of the microstructure of the material, and the inherent spatial randomness.

The effective medium theories allow direct estimations of effective properties. Eshelby [15] proposed the *equivalent inclusion method* to calculate the effective properties of the composite. The method involves assuming one phase as the matrix, and the second phase as the inclusions. The inclusion's shapes are described by regular geometry which can vary from being a sphere or penny shape to a rod. One theory by Mori-Tanaka [33] models one phase as a matrix, the second phase as randomly distributed inclusions, and calculates the average stress field in the matrix. All these theories assume that the heterogeneous materials have an isotropic matrix phase having well defined shear and bulk moduli. This assumption is invalid in case of polycrystals which is an aggregate of different phases with different properties. To circumvent this problem, *self-consistent method* was proposed [23, 9]. These methods assume that one of the phases (inclusions), can be described by a regular geometry, and thus are just a function of volume fraction of one of the phases. Again, these methods are independent of the spatial randomness inherent in the microstructure.

Micromechanics studies of heterogeneous materials are done with the goal of determining the effective properties of such materials using constitutive laws and spatial distributions of the present individual phases. Homogenization as a technique is the best-known way, which is used to estimate the effective properties of

heterogeneous materials with varying microstructures. Here we define the mesoscale (δ), which is a non dimensional parameter used to characterize the scale of observation as: $\delta = L/d$. L is the macro scale, and d is the micro scale of the order of the size of the material particle. Separation os scales (Micro (d), Meso (δ), Macro (L)), in these microstructures leads to the problem of determination of Representative Volume Element (RVE) that corresponds to the effective properties of materials. The RVE for a heterogeneous material system is defined as a volume V, which is statistically large enough to include *all* microstructural hetrogeneities of a composite, and small enough to be considered as a volume element in continuum mechanics. Not much attention in literature has been paid to the determination of the size of the so-called Representative Volume Element (RVE). This is because most engineering applications are designed to function above the RVE. With the advent of nanotechnology, this is not the case anymore. Damage and fracture phenomenon in multi-phase microstructure take place at scale well below the RVE size. Hence, it becomes extremely essential to study the responses of these microstructures below RVE. Similar work using Hill-Mandel condition has been used to homogenize a two-phase 3d Voronoi mosaic for linear elasticity and thermal conductivity [22].

Since, microstructural randomness is inherent in these materials, hence we study the scaling from the Statistical Volume Element (SVE) to the RVE. Using the Hill-Mandel condition, the RVE is achieved when the material response becomes independent of the two boundary conditions (kinematic and static boundary condition) setup on the SVE. In essence this involves solving the two stochastic boundary value problems on the random microstructure (see §1.2.1). As we increase the number of grains (scale up in size), we move from the SVE and begin to approach the RVE response. At sufficiently large scales, the response of the material becomes independent of the two applied boundary conditions (kinematic and static boundary condition). This methodology gives us scale dependent bounds on the random microstructure. While this approach has its simpler parallel in conductivity of random materials [37, 45], it has been used for (non)linear (thermo)elastic and inelastic, and permeable material problems [14, 22, 50].

1.2 Homogenization of elastic response

As is well known, the rules of mixtures given by Voigt [56] and Reuss [48] provide the upper and lower bound of response of a multi-phase material. In a two-phase material with given volume fraction of each phase, the shear response is bounded as follows:

$$\mu_{eff} = \mu_1 V_f + \mu_2 (1 - V_f) \tag{1.1}$$

$$\frac{1}{\mu_{eff}} = \frac{V_f}{\mu_1} + \frac{1 - V_f}{\mu_2} \tag{1.2}$$

Hashin-Shtrikman[17] improved upon these bounds and provided bounds on the shear response as follows:

$$\mu_{upper} = \mu_1 + \frac{1 - V_f}{\frac{1}{\mu_2 - \mu_1} + \frac{6(K_1 + 2\mu_1)V_f}{5\mu_1(3K_1 + 4\mu_1)}} \tag{1.3}$$

$$\mu_{lower} = \mu_2 + \frac{V_f}{\frac{1}{\mu_1 - \mu_2} + \frac{6(K_2 + 2\mu_2)(1 - V_f)}{5\mu_2(3K_2 + 4\mu_2)}} \tag{1.4}$$

Figure 1.1 shows the variation in these bounds as a function of volume fraction of one of the phases. The two phases represented in this figure have a contrast of 10 in their shear modulus. As we can see the Voigt-Reuss bounds are far wider, and the Hashin-Shtrikman provide tighter bounds. One important thing to observe here is that both these bounds depend only on the volume fraction of each phase, and hence are scale independent. We cannot identify the size of the RVE from these bounds, and the inherent randomness in microstructure, which characterizes these bounds at different scales, is lost.

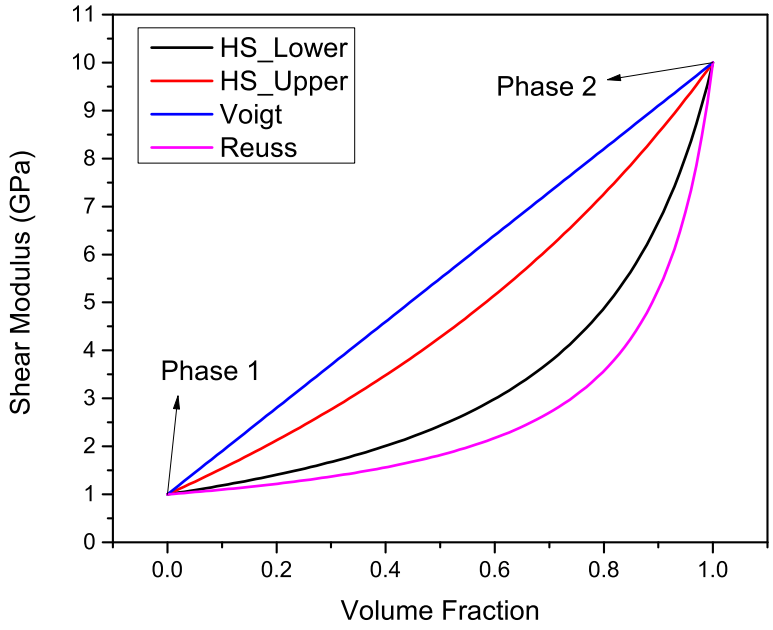

Figure 1.1: Effective shear modulus for a two-phase microstructure as a function of volume fraction

Since, identification of the size of the RVE is one of the primary goals of this research, hence we perform

multi-scale simulations based on Hill-Mandel macrohomogenity condition [19]. Our simulations as a result produce scale dependent bounds on the effective properties of the microstructure without losing it's inherent random characteristics.

1.2.1 A note on Hill-Mandel condition

The Hill-Mandel condition establishes an equivalence between the energetic and mechanical approaches for setting up constitutive relations such that,

$$\overline{\sigma_{ij} : \varepsilon_{ij}} = \overline{\sigma_{ij}} : \overline{\varepsilon_{ij}} \tag{1.5}$$

σ_{ij} and ε_{ij} represent the Cauchy stress and strain tensor respectively. The equation (1.5) is valid provided any of the following boundary conditions are satisfied,

1. Uniform displacement boundary condition (Dirichlet)

$$u_i = \varepsilon^0_{ij} x_j \tag{1.6}$$

2. Uniform traction boundary condition (Neumann)

$$t_i = \sigma^0_{ij} n_j \tag{1.7}$$

By increasing the mesoscale (δ), and setting up stochastic boundary value problems with above boundary conditions, and upon ensemble averaging, one obtains bounds on the constitutive response of the microstructure.

1.3 Thesis Outline

The research presented in this thesis is organized into the following chapters:

⇒ In Chapter 2, we perform the homogenization based on the Hill-Mandel macrohomogenity condition on two-phase random checkerboard type of microstructure. We validate our simulations using existing analytical relations. We then proceed to perform the multi-scale simulations as a function of volume fraction of one of the two phases. We then present our results for two different contrast in the material properties of the two phases present in the microstructure.

⇒ Chapter 3 extends this homogenization tool to a different two-phase microstructure. We then present a tool to generate a Gaussian correlated microstructure with isotropic correlations. We perform our simulations for different contrasts in the material properties of the two phases, and also for different correlation lengths. We then propose scaling functions for the shear modulus of the microstructure. We also present a comparison of our numerical results with the experimental study on Nickel-Alumina composites with correlated microstructure.

⇒ Chapter 4 is an introduction to fractals. We present certain existing methodologies to quantify fractals and estimate their dimension. We also study how fractals have been used in evolution of plasticity in materials.

⇒ In Chapter 5, we deal with a unique microstructure called FGM (Functionally graded materials). The material system in consideration is Ti-TiB (metal-ceramic). We present the non-uniqueness in the homogenization of these microstructures in 3d. We then study the elastic-plastic transitions in these microstructures, and how the material response is sensitive to the applied boundary conditions. We then present the use of fractals as a tool to measure evolving plasticity in the microstructure.

⇒ Chapter 6 summarizes the research with main conclusions. Discussion on future direction of this research is also presented.

Chapter 2

Random Checkerboard

One of the most simple example of a random composite is a random checkerboard. The random checkerboard has been of great interest and widely studied under anti-plane elasticity [12], and planar elasticity [44]. The random checkerboard can also be an example of a correlated microstructure with *zero* correlation length. The correlated microstructures are discussed in detail in Chapter 3. An example of a two-phase random checkerboard is shown in Fig. 2.1.

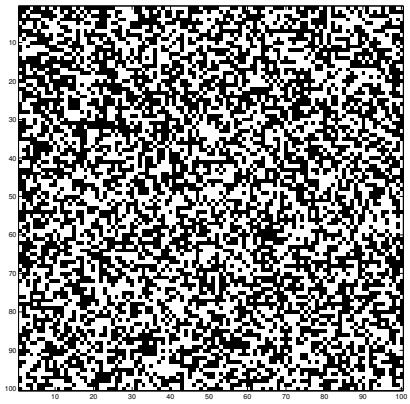

Figure 2.1: Random two-phase checkerboard composite at 50% volume fraction

The properties of this composite depends on the properties of the individual phases, their volume fractions, and the scale of observation. Continuum mechanics provides concepts under which *'separation of scales'* is often invoked. However, when random composites are taken into consideration the *'separation of scales'* does not necessarily exists. Especially with the advent of MEMS and NEMS technology, the study of homogenization of these composites has become extremely significant since at those scales we might run the risk of functioning below the RVE scale.Various homogenization studies under Hill-Mandel conditions have been carried out [36].

2.1 Model formulation

A microstructure is formulated which is composed of randomly arranged perfectly bonded isotropic single grains. Each point in the microstructure is occupied by either of one the two phases as shown in the Fig. 2.1.

In effect, we would have a random material $\mathcal{B} = \{\mathcal{B}(\omega); \omega \in \Omega\}$, where each realization has a deterministic mechanics governed only by the contrast in their material properties.

$$k = \frac{E_{black}}{E_{white}} \tag{2.1}$$

The indicator function of this microstrucutre can be characterized by,

$$\chi(\omega, x) = \begin{cases} 1 & if x \in \mathcal{B}_{black} \\ 0 & if x \in \mathcal{B}_{white} \end{cases} \quad ; \chi : \Omega \times \mathbb{R}^2 \to \{0, 1\} \tag{2.2}$$

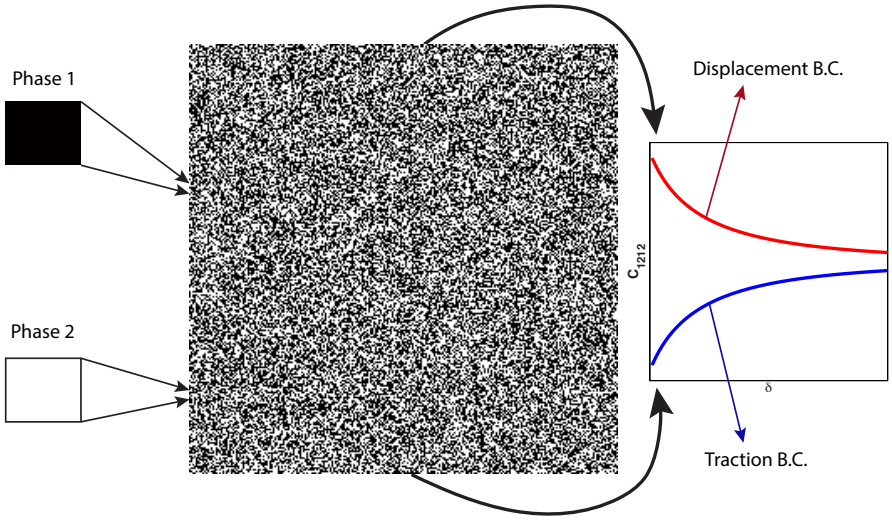

Figure 2.2: Homogenization procedure for random checkerboard type microstructures

The numerical simulations are carried out for a phase contrast of 2.1 at 50% volume fraction as discussed in §2.2. After validating our numerical results, we move on to carry out out numerical analysis for a higher phase contrast, and at different volume fractions (see §2.3).

2.2 Benchmark test

Benchmark simulations are performed on the microstructures for which the effective response can be computed analytically. This helps in validating our FEM calculations which we use to solve the stochastic boundary value problems (see §1.2.1). For two-phase microstructures consisting of isotropic phases and having equal bulk moduli ($K_1 = K_2 = K_*$), the effective shear moduli ($\mu_{effective}$) is given by [31]:

$$K_* = K, \mu_{effective}(\mu_1, \mu_2, K) = \frac{K}{-1 + \sqrt{(1 + K/\mu_1)(1 + K/\mu_2)}} \tag{2.3}$$

where μ_1 and μ_2 are the shear moduli of the two phases of the microstructures. The scale dependence of shear moduli in random checkerboard is shown in Fig. 2.3. Figure 2.3 shows that response from the two boundary conditions (see §1.2.1) converges to the analytical value. The analytical value was computed using equation (2.3) and values taken from Table 2.1. It can be inferred that the bounds will collapse to the analytical value at infinite mesoscales.

The uniform kinematic and uniform static boundary value problems are solved using equations (1.6) and (1.7). As a result we obtain the bounds on the aggregate shear response (Fig. 2.2) of the microstructure which converges to the relation as defined by equation (2.3), for $k = 2.1$.

Properties	**Young's modulus (E) GPa**	**Poisson's ratio (ν)**	**Bulk modulus (K) GPa**	**Shear modulus (μ) GPa**
Phase 1	1	0.3	0.8333	0.3846
Phase 2	2.1	0.08	0.8333	0.9722

Table 2.1: Material parameters for a random two phase checkerboard with k=2.1

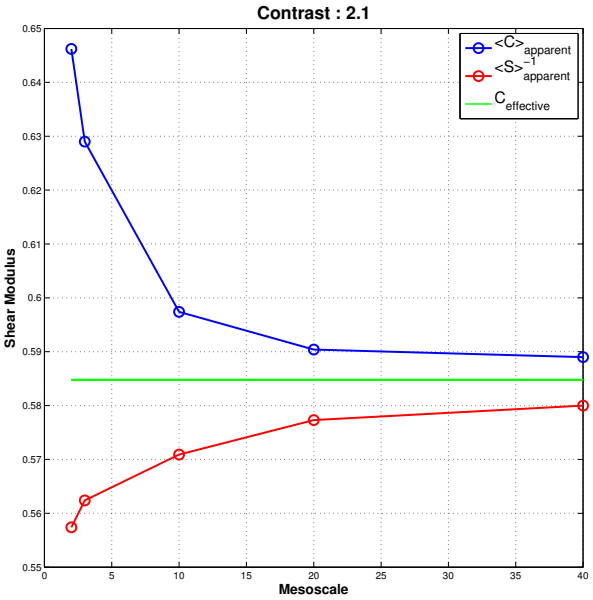

Figure 2.3: Shear response of a random checkerboard as a function of mesoscale (δ)

The analytical value calculated using material parameters given in Table 2.1, and equation (2.3) is $\mu_{effective} = 0.5848$ (denoted by green line in Fig. 2.3). As we can observe from Fig. 2.3, the bounds converge to the analytical value of the equivalent shear response given by equation (2.3), which validates our model. The values are tabulated in Table 2.2.

Mesoscale (δ)	$\langle C_{app} \rangle$	$\langle S_{app}^{-1} \rangle$	**# of simulations**	**Error (%)**
2	0.6462	0.5574	16	10.5 (4.7)
3	0.6290	0.5624	512	7.5 (3.8)
10	0.5974	0.5709	150	2.1 (2.3)
20	0.5904	0.5773	150	0.9 (1.3)
40	0.5890	0.5800	150	0.7 (0.8)

Table 2.2: Numerical results for different mesoscales at k=2.1 showing decreasing errors with increasing mesoscales. The errors in bracket represents relative error of $\langle S_{app}^{-1} \rangle$ with the analytical value

2.3 Numerical simulations

We further perform another set of analysis with a stronger contrast in the material properties of the two phases (k=10) as given in Table 2.3. For a higher contrast we expect to see a weak homogenization i.e. the bounds from the two boundary value problems (equations (1.6) and (1.7)) converge at a higher mesoscale (δ).

Properties	**Young's modulus (E) GPa**	**Poisson's ratio (ν)**	**Shear modulus (μ) GPa**
Phase 1	100	0.3	38.46
Phase 2	1000	0.3	384.6

Table 2.3: Material parameters for a random two phase checkerboard with k=10

The numerical tests were carried out for a range of volume fractions from 0% volume fraction to 100% volume fraction in steps of 10. The corresponding mesoscale (δ) range for these tests were from 10 to 300. Sample realizations at $\delta = 10$, and 300 for different volume fractions are shown in Fig. 2.4.

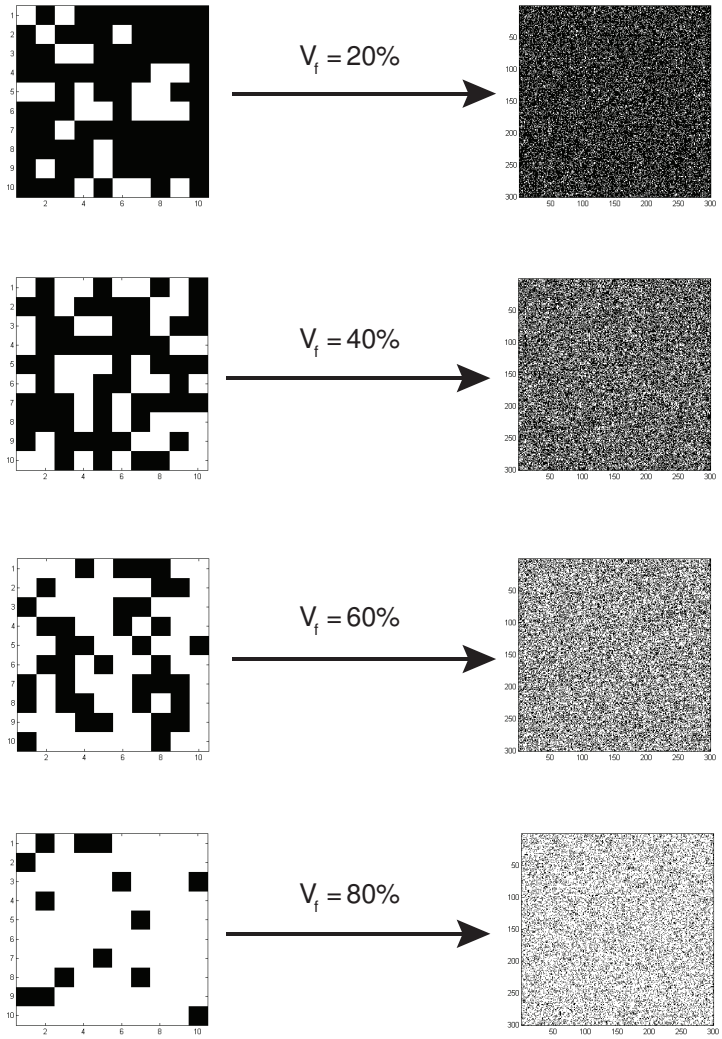

Figure 2.4: Sample realizations at $\delta = 10$ and 300 for increasing volume fraction of the white phase.

The bounds on the response of the material was plotted as a function of volume fraction for different values of δ (see Fig. 2.5).

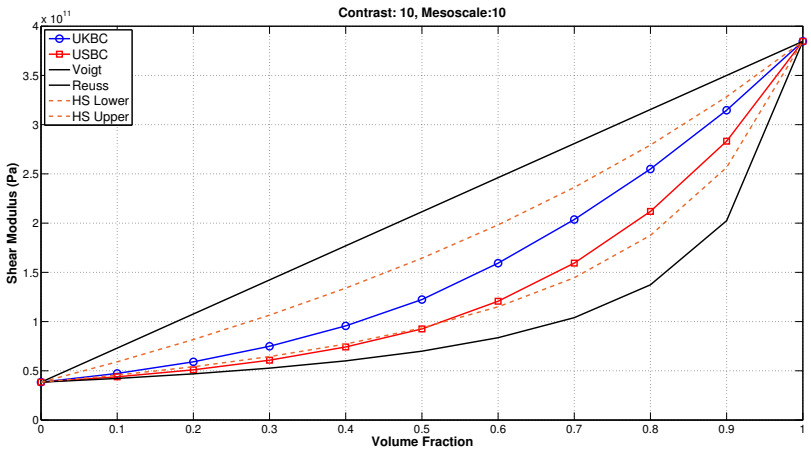

(a)

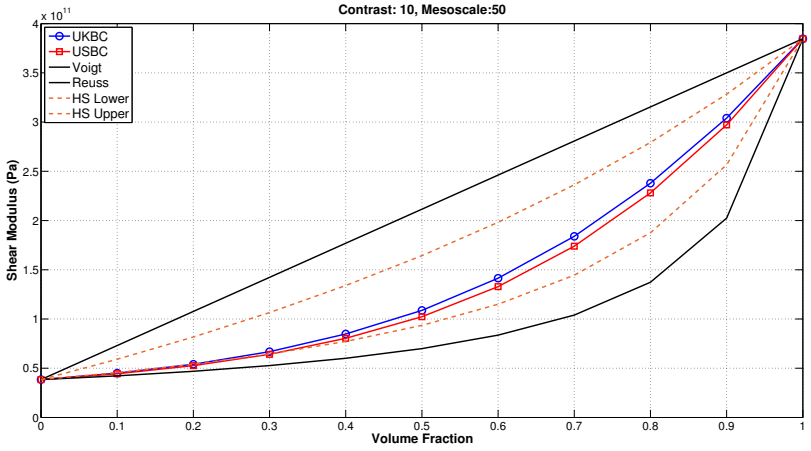

(b)

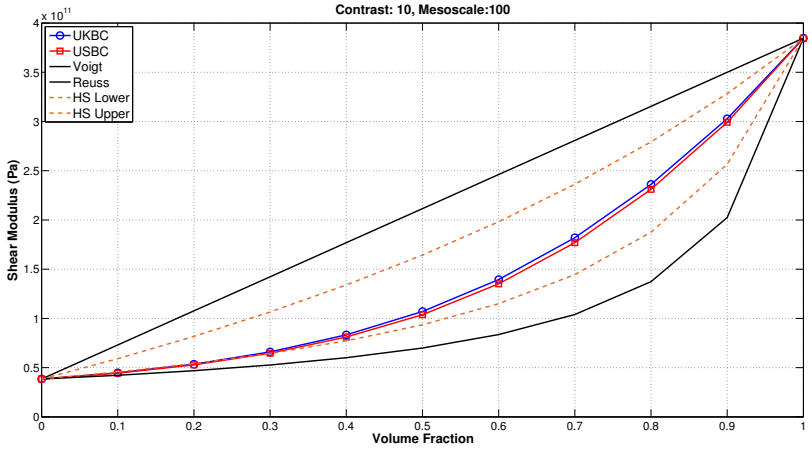

(c)

Figure 2.5 (cont. on next page).

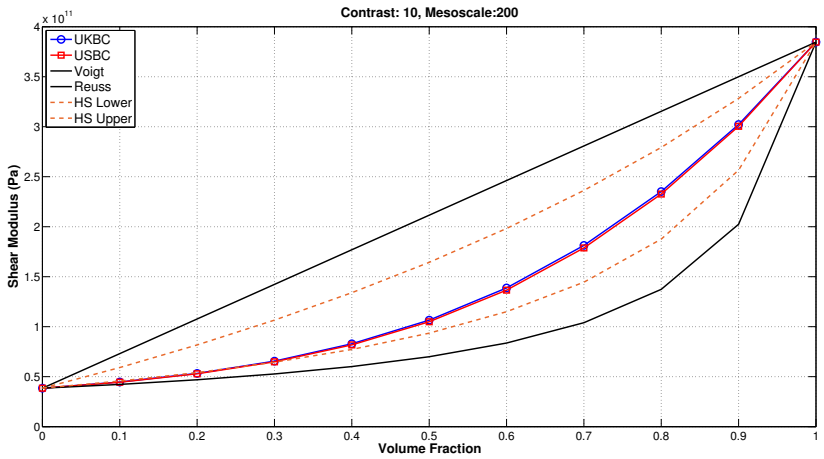

(d)

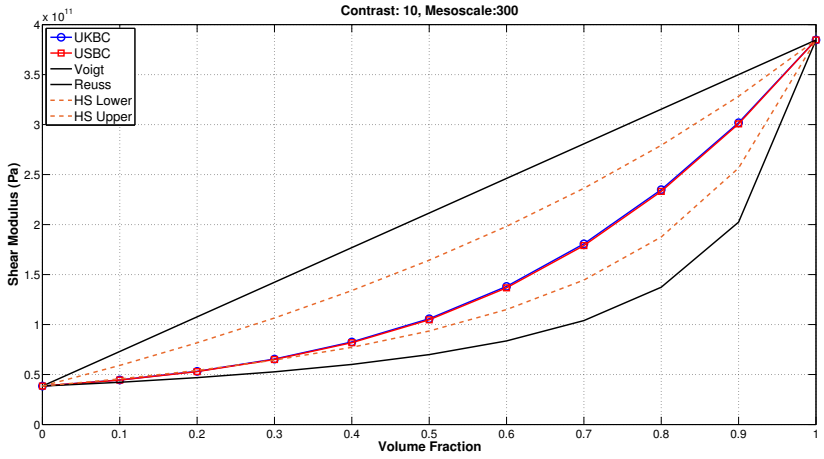

(e)

Figure 2.5: Homogenization of material response for different volume fractions at (a) δ=10, (b) δ=50, (c) δ=100, (d) δ=200, and (e) δ=300.

As we can see from Figs. 2.5(a) - 2.5(e), the bounds of the material response get tighter as we increase our mesoscale (δ) from 10 to 300. To better look at the convergence of the bounds as a function of δ, we choose volume fraction of 50% to capture the trend as shown in Fig. 2.6.

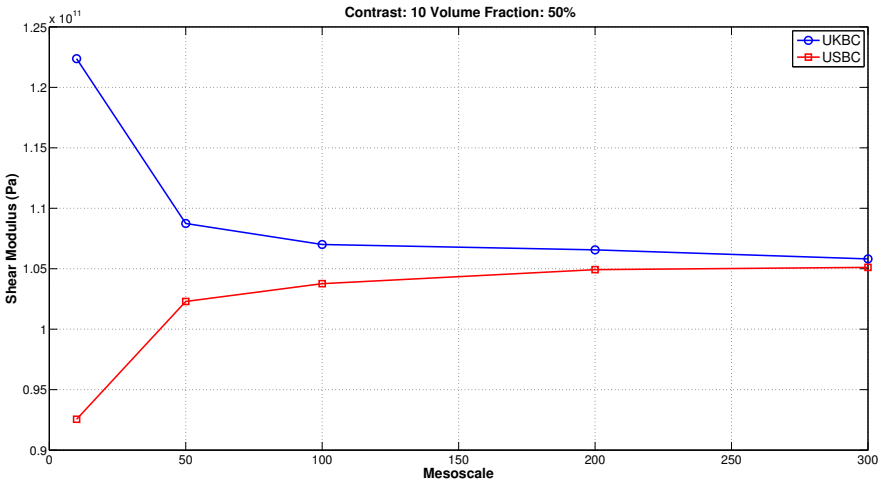

Figure 2.6: Shear response of a random checkerboard as a function of mesoscale (δ) for k=10

As expected, it is clear from Fig. 2.6, that bounds are converging at a higher value of mesoscale (δ). These bounds are predicted to collapse to a point when $\delta \to \infty$,however for the sake of numerical accuracy we stop our simulations at δ=300. Thus, we can say that when δ=300, we achieve the RVE response of the microstructure as the difference between the bounds is $\sim 0.67\%$.

Chapter 3

Gaussian Correlated Microstructures

Most microstructures of heterogeneous materials are not exactly random (i.e. white noise random fields). They display some clustering of hetrogeneities, as can be described by the correlation function. Experimental studies on Pb-Sn alloys (see Fig. 3.1 [21]) have revealed that the distribution of the hetrogeneities can be well explained with a Gaussian correlation function. In general, the presence of short range spatial correlations (like Gaussian) in the phase distribution imparts a length scale that can be identified as the correlation length λ of the microstructure. In the case of a random microstructure, $\lambda \approx d$, where d is the microscale defined as the length scale at which independent phases of the microstructure can be identified. But, when finite spatial correlations exist, λ is greater than d and can affect the overall mechanical properties of the composite material. The scale dependent homogenization studies of mechanical or thermal responses conducted in the past were limited mostly to random microstructures, where transition from the SVE to the RVE was studied as a function of δ. Therefore, to understand how the presence of spatial correlations controlled by the length scale λ, in addition to the mesoscale δ, affects the transition from the SVE to the RVE, and the effective properties of two-phase composite materials is the objective of this study. In this chapter, we obtain scale dependent bounds for the Gaussian correlated microstructure to understand the role of the correlation length scale on the transition from the SVE to the RVE.

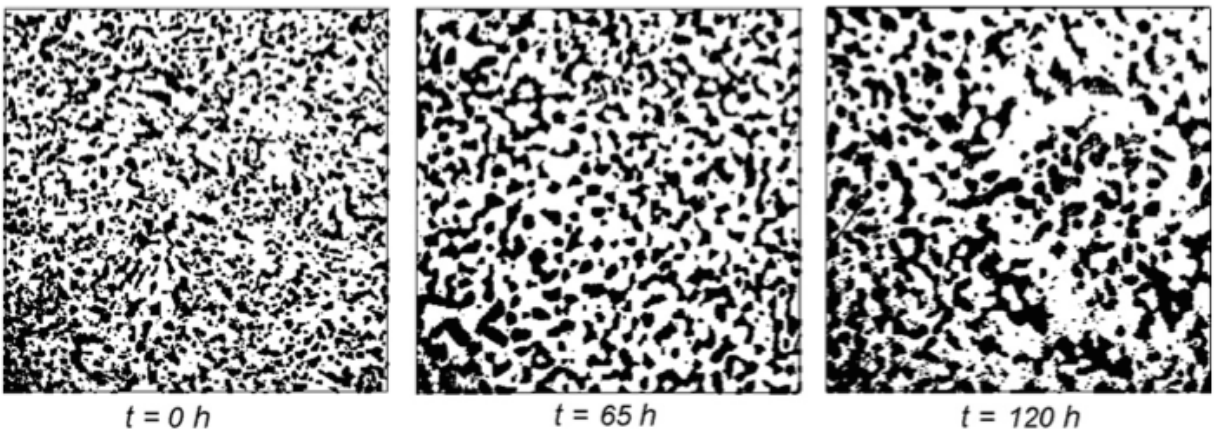

Figure 3.1: 2d images of Pb37Sn63 alloy samples isothermally aged at different time periods. The scale of the images is of order $\sim 200\mu$m [21]

3.1 Microstructure formulation

Gaussian correlations are short range correlations, which mimic the particle size influence in the percolation of the two-phase microstructure. The auto-correlation function (R) of a random variable (f) is the measure of the 'memory' or influence of an event at r, on that of an event at $r + \widetilde{r}$.

$$R(r) \coloneqq \langle f(r) f(r + \widetilde{r}) \rangle \tag{3.1}$$

If function $f(r)$ is assumed to be a stationary random field then it's mean ($\langle f \rangle$) is constant. The normalized auto-correlation function is then given by,

$$\rho(r) \coloneqq \frac{R(r)}{\sigma^2} \tag{3.2}$$

Where, σ is the standard deviation. The normalized auto-correlation function (ρ) varies from a maximum of 1 at $\widetilde{r} = 0$, (meaning every point correlates perfectly with itself), and decays to 0 as $r \to \infty$, meaning it does not influence the presence of a particle at $\widetilde{r} = \infty$. The Gaussian correlation function is given by [36]:

$$\rho(x, y) = e^{-\gamma_1 x^2 - \gamma_2 y^2} \tag{3.3}$$

For isotropic correlations (x- and y- correlate identically spatially), we have $\gamma_1 = \gamma_2$. Then (3.3) reduces to the following form,

$$\rho(r) = e^{-\gamma r^2} \tag{3.4}$$

Where, r can be defined as,

$$r = \sqrt{x^2 + y^2} \tag{3.5}$$

And γ is related to the correlation length (λ) by:

$$\gamma = \frac{1}{2l^2} = \frac{\pi}{4\lambda^2} \tag{3.6}$$

$$\lambda = \int_0^\infty \rho(r)\, \mathrm{d}r \tag{3.7}$$

Further, the spread (influence) of correlation functions is quantified by the integral length scale, λ, as given by equation (3.6). For an isotropic distribution we would have $\gamma_1 = \gamma_2$. The two-phase microstructure (Fig. 3.2) is then generated from the correlation function given by equation (3.4) using an algorithm given by Makse *et al.* [28] (see appendix A[1])

[1] Prepared by Sohan Kale

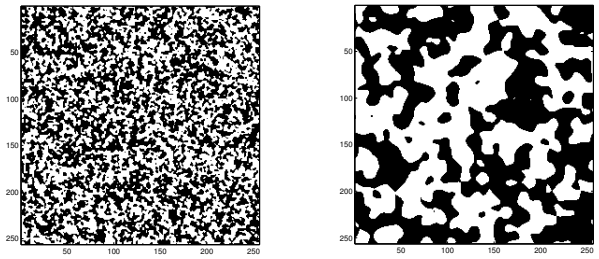

(a) (b)

Figure 3.2: Gaussian correlated distribution for δ=256 at 50% volume fraction (a) λ=2, (b) λ=8

Hence, we can generate two phase microstructure with two characteristic length scales namely, mesoscale (δ), and the correlation length (λ). Indeed the correlation length (λ) serves as a resolution operator on the mesoscale (δ) window as can bee seen from Fig. 3.2. It is to be noted that as $\lambda \to 0$, we retrieve an uncorrelated microstructure like a random checkerboard which was discussed in Chapter 2.

3.2 Computational Procedure

The microstructure is made of perfectly bonded isotropic single grains, where each point is occupied by either one of the two phases as shown is Fig. 3.2.

In effect, we have a random material $\mathcal{B} = \{\mathcal{B}(\omega); \omega \in \Omega\}$, where each realization follows the laws of deterministic mechanics with spatial disorder described, besides the random geometry, by the contrast in material properties:

$$k = \frac{E_{black}}{E_{white}}. \tag{3.8}$$

The uniform kinematic and uniform static boundary value problems are solved using equations (1.6) and (1.7).

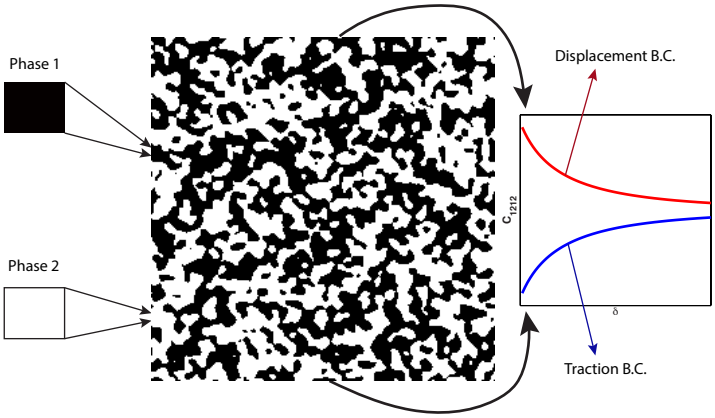

Figure 3.3: Homogenization procedure for correlated microstructures

Numerical experiments using finite elements are carried out (see Table 3.1) on a sample set of two-phase Gaussian correlated microstructures for varying mesoscale ($\delta = 4, 8, 16, .., 512$), contrast ($k = 2, 4, 8$) and correlation lengths ($\lambda = 1, 2, 4, 8, 16$).

For every microstructure, two tests are run to determine the in-plane shear components of the stiffness and compliance tensors from the strain energy density given in Eqs. (3.9) and (3.10), respectively.

$$U_\delta^d = \frac{V}{2}\overline{\sigma_{ij}}\varepsilon_{ij}^0 = \frac{V}{2}[4C_{1212}(\varepsilon_{12}^0)^2], \tag{3.9}$$

$$U_\delta^t = \frac{V}{2}\overline{\varepsilon_{ij}}\sigma_{ij}^0 = \frac{V}{2}[4S_{1212}(\sigma_{12}^0)^2]. \tag{3.10}$$

Contrast (k)	λ	δ
2,4,8	1,2,4,8,16	4
		8
		16
		32
		64
		128
		256
		512

Table 3.1: Input parameters for numerical simulations at nominal volume fraction of 50%

3.3 Comparison with experimental studies

The correlated microstructures studied are then compared numerically with the experimental studies conducted by Aldrich *et al.* [2] using the methodology discussed in §1.2.1. They studied the micrographs of Nickel and Alumina composites. The micrographs thus obtained were a close match to Gaussian correlated microstructure (see Fig. 3.4). Similar numerical studies were performed for a functionally graded microstructure as a function of volume fraction [55].

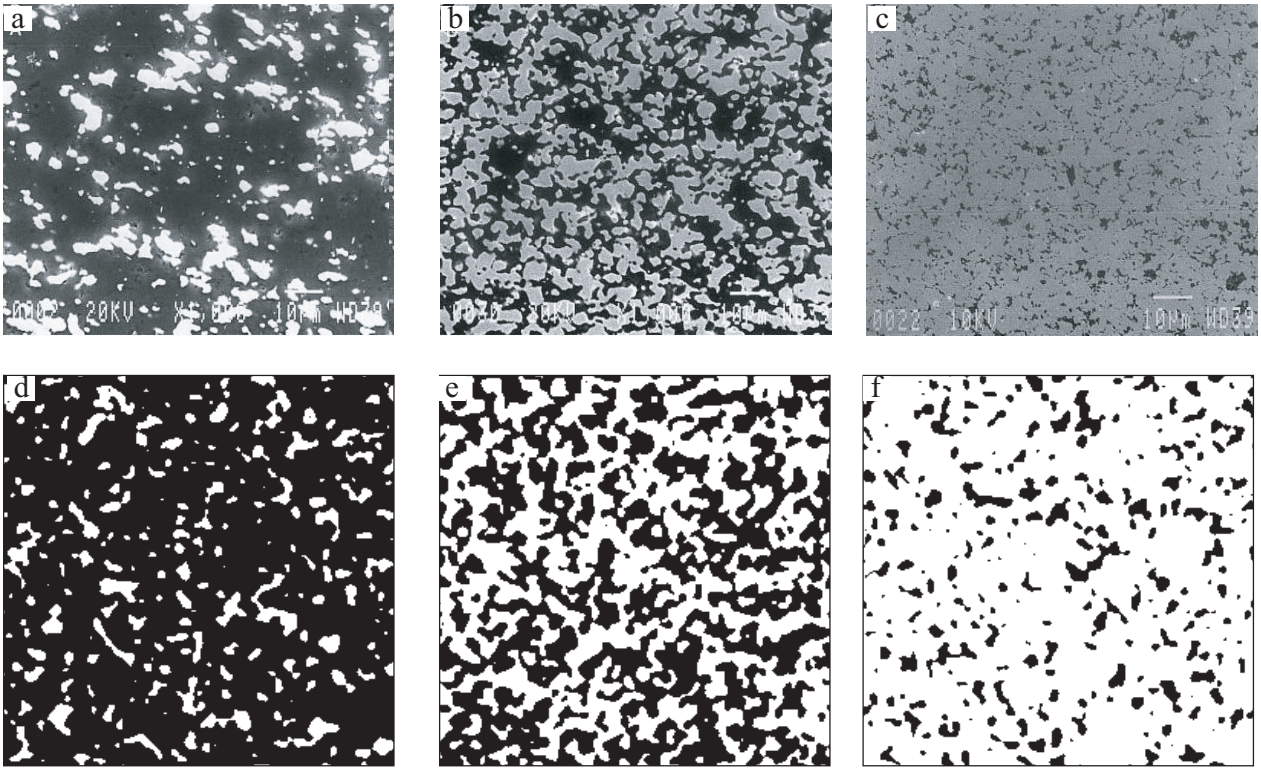

Figure 3.4: Actual SEM micrographs [2] of Al_2O_3/Ni at volume fraction (a) 15% Ni, (b) 50% Ni, (c) 85% Ni; Generated samples of correlated microstructure by our methodology for volume fraction (d) 15% Ni, (e) 50% Ni, (f) 85% Ni.

Young's modulus of Alumina and Nickel were taken to be 393 and 207 GPa respectively. The Poisson ratio for Alumina and Nickel was 0.31 and 0.22 respectively [2]. The experimental study calculated Poisson's ratio using the following equation:

$$\nu_{eff} = \nu_I f_I + \nu_{II} f_{II} \tag{3.11}$$

Where f_I and f_{II} represent the volume fractions of Alumina and Nickel respectively. The results of the comparison with the experimental data are presented in Fig. 3.5. The shear modulus for the composite data is calculated using the following equation:

$$G_{eff} = \frac{E_{eff}}{2(1+\nu_{eff})} \tag{3.12}$$

The experimentally obtained values of Young's modulus are tabulated in Table 3.2.

Vol. fraction of Ni	Young's modulus (E) GPa
15%	354.2
25%	326.1
35%	297.7
50%	296.2
65%	269.1
85%	226.5

Table 3.2: Experimentally obtained Young's modulus for Nickel and Alumina composites [2]

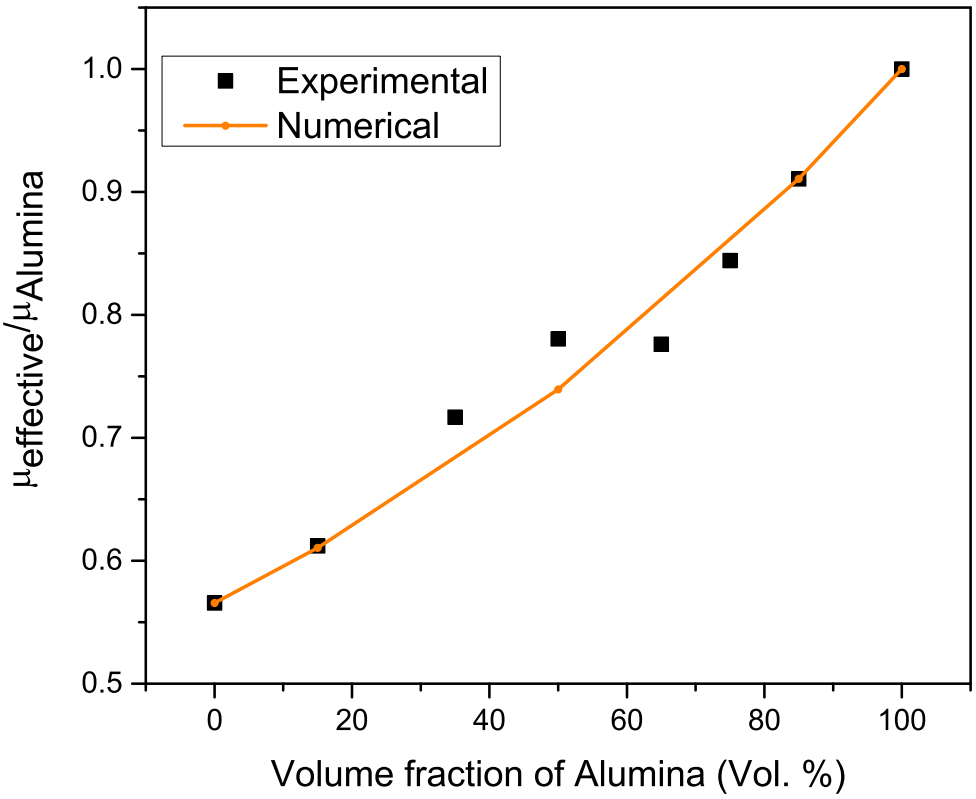

Figure 3.5: Normalized shear modulus of the composite as a function of volume fraction of Al_2O_3.

As can be observed from Fig. 3.5, our numerical model results match the experimental data very closely. Due to the expensive nature for the simulations, we consider these three volume fractions $V_f = 15\%, 50\%, 85\%$ for alumina. For volume fraction 50%, the deviation can be attributed to a combination of factors such as

statistical error, inaccurate calculation of Poisson's ratio (equation (3.11)). For volume fraction 15%, and 85% since the material microstructure is pretty much homogeneous, hence errors due to factors stated above are assumed to be minimal.

3.4 Formulation of the scaling function

We introduce the scaling function covering the entire range of $\delta \in [1, \infty)$. It is assumed that the scaling function spans different length scales. For the isotropic case we have, $C_{1212} = S_{1212}^{-1} = \mu$ Solving the boundary value problem under the condition (1.6), we can obtain mesoscale shear stiffness by

$$\overline{\sigma_\delta}(\omega) = C_\delta^d : \varepsilon^0 \tag{3.13}$$

Similarly, solving boundary value problem under condition (1.7), we can obtain mesoscale shear compliance by

$$\overline{\varepsilon_\delta}(\omega) = S_\delta^t : \sigma^0 \tag{3.14}$$

Using equations (3.13) and (3.14), we obtain

$$\langle C_\delta^d \rangle : \langle S_\delta^t \rangle = \frac{\langle \mu_\delta^d \rangle}{\langle \mu_\delta^t \rangle} \tag{3.15}$$

In the limit $\delta \to \infty$, the compliance shear must be the exact inverse of the stiffness shear, which yields,

$$\lim_{\delta \to \infty} \langle C_\delta^d \rangle : \langle S_\delta^t \rangle = 1 \tag{3.16}$$

Using equations (3.15) and (3.16), the following relationship is proposed:

$$\langle C_\delta^d \rangle : \langle S_\delta^t \rangle = \lim_{\delta \to \infty} \langle C_\delta^d \rangle : \langle S_\delta^t \rangle + f(k, \mu_1, \mu_2, \delta) \tag{3.17}$$

where μ_1 and μ_2 represent the shear moduli of the individual phases, and $f(k, \mu_1, \mu_2, \delta)$ defines the scaling function. Substituting (3.16) to (3.17), we obtain:

$$f(k, \mu_1, \mu_2, \delta) = \frac{\langle \mu_\delta^d \rangle}{\langle \mu_\delta^t \rangle} - 1 \tag{3.18}$$

This scaling function has the following property,

$$f(k, \mu_1, \mu_2, \infty) = 0 \tag{3.19}$$

The above equation holds because when $\delta \to \infty$, the traction and displacement controlled shear moduli are identical. At $\delta = 1$, the displacement and traction controlled shear moduli are equal to the Voigt and Reuss estimates (denoted by superscripts $'V'$ and $'R'$).

$$f(k, \mu_1, \mu_2, 1) = \frac{\mu^V}{\mu^R} \tag{3.20}$$

Equations (3.19) and (3.20) impose the following bounds on the scaling function:

$$0 \leq f(k, \mu_1, \mu_2, \delta) \leq f(k, \mu_1, \mu_2, 1) \tag{3.21}$$

As a consequence of equation (3.21), a *normalized scaling function* can be introduced, such that

$$0 \leq g(k, \mu_1, \mu_2, \delta) = \frac{\frac{\langle \mu_\delta^d \rangle}{\langle \mu_\delta^t \rangle} - 1}{\frac{\mu^V}{\mu^R} - 1} \leq 1 \tag{3.22}$$

The functional form of the scaling function would be obtained by curve fitting the normalized scaling function (which is the mean of equation (3.22) for all microstructures). A *stretched exponential* function was found to be a good fit for 3d elastic polycrystals [46]. This scaling function can prove to be helpful in determining the RVE size of a random microstructure at a given phase contrast (k) since it is a function of the mesoscale (δ).

3.5 Numerical results

For a given k and λ, we use a large number of realizations $N_\delta = \{150, 150, 150, 150, 50, 25, 10\}$ for $\delta = \{4, 8, 16, 64, 128, 256, 512\}$, respectively. For each realization $\mathcal{B}(\omega)$ at a given δ, we get C^δ_{1212} and S^δ_{1212} using the boundary conditions given in equations (1.6) and (1.7), respectively. Upon averaging over N_δ realizations we obtain the upper bound $\langle C^\delta_{1212} \rangle$ and lower bound $\langle S^\delta_{1212} \rangle^{-1}$ on $\langle C^{eff}_{1212} \rangle$ as shown in Fig. 3.6 for $\lambda = \{1, 2, 4, 8, 16\}$. Two trends can be observed here: (1) an increasing k results in a slower approach to the RVE, and (2) an increasing λ also results in a slower approach to the RVE.

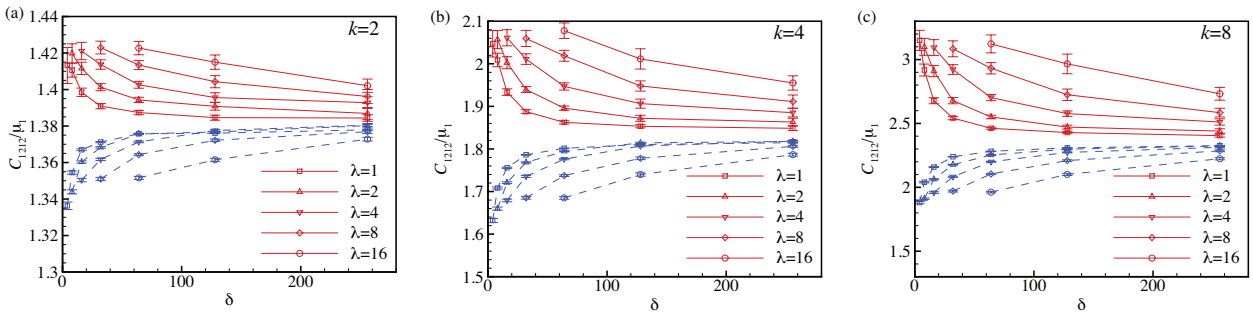

Figure 3.6: $\langle C^d_\delta \rangle$ (blue) and $\langle S^t_\delta \rangle^{-1}$ (red) at λ=1,2,4,8,16 for (a) k=2, (b) k=4 and (c) k=8.

The bounds obtained in Fig. 3.6 can be collapsed by normalizing the mesoscale (δ) by the correlation length (λ) (see Fig. 3.7).

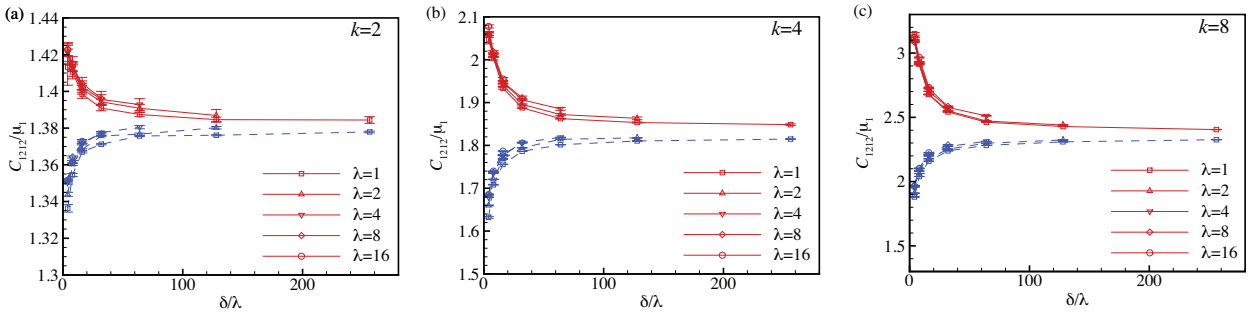

Figure 3.7: $\langle C^d_{\delta/\lambda} \rangle$ (blue) and $\langle S^t_{\delta/\lambda} \rangle^{-1}$ (red) at λ=1,2,4,8,16 for (a) k=2, (b) k=4 and (c) k=8.

Using equation (3.18) the scaling functions $f(\delta/\lambda, k)$ are obtained for different contrast values ($k = 2, 4, 8$) at different λ as shown in Fig. 3.8. Similar to Fig. 3.7, the scaling functions for different λ can also be collapsed by plotting as a function of δ/λ. Thus, we can use the scaling function obtained for the smallest correlation length considered (*i.e.* $\lambda = 1$) as a representative of all other λ values for further analysis. The advantage of this approach is that, with smaller λ, the bounds converge at much lower values of δ, and therefore, we do not need to simulate systems at large λ values which would require much larger δ values to converge.

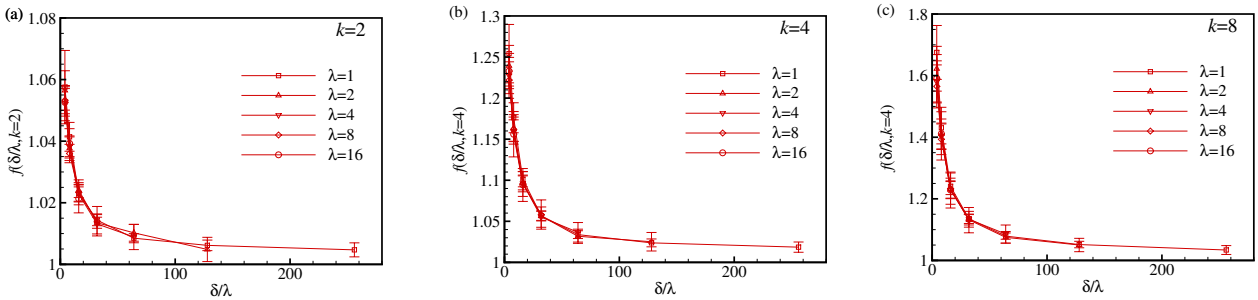

Figure 3.8: The scaling function $f(\delta/\lambda, k)$ as defined in equation (3.18) plotted against δ/λ for (a) k=2, (b) k=4 and (c) k=8. Each subfigure has curves corresponding to $\lambda = 1, 2, 4, 8, 16$ that can be observed to collapse well.

The normalized scaling function is obtained using the equation (3.22), and the scaling function obtained for $\lambda = 1$ at $k = 3, 4, 8, 32, 64, 128$, is shown in Fig. 3.9. The normalized scaling function curves for different λ and k values are not collapsing well as expected after rescaling the mesoscale as δ/λ.

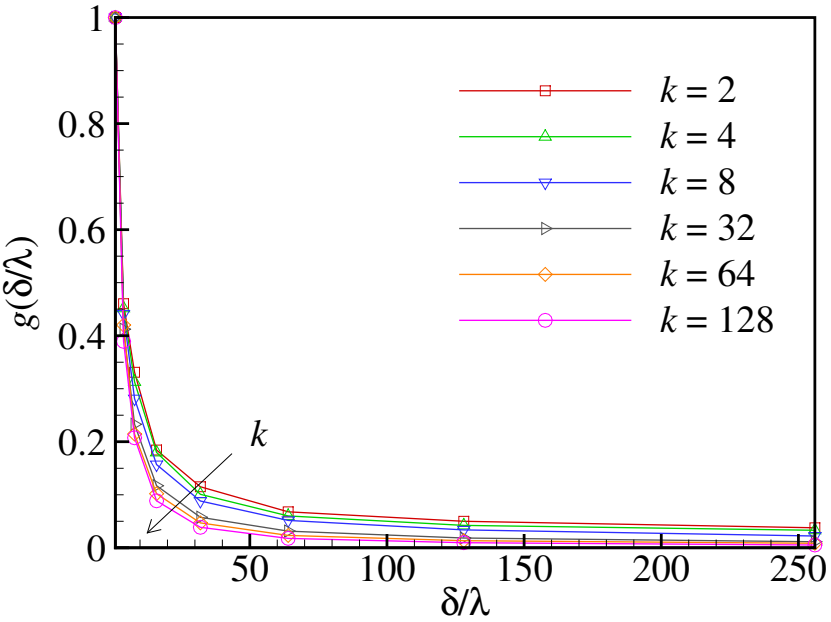

Figure 3.9: Normalized scaling function $g(\delta, \lambda)$ plotted against δ/λ for different phase contrasts (k).

It is clear from Fig. 3.9 that the normalized scaling function thus obtained is still a function of contrast between the two phases as can be clearly seen in the downward shift with increasing phase contrast in the same. To make this more apparent, we plot the normalized scaling function for the two extreme phase contrasts (Fig. 3.10), where this downward shift can be more clearly seen.

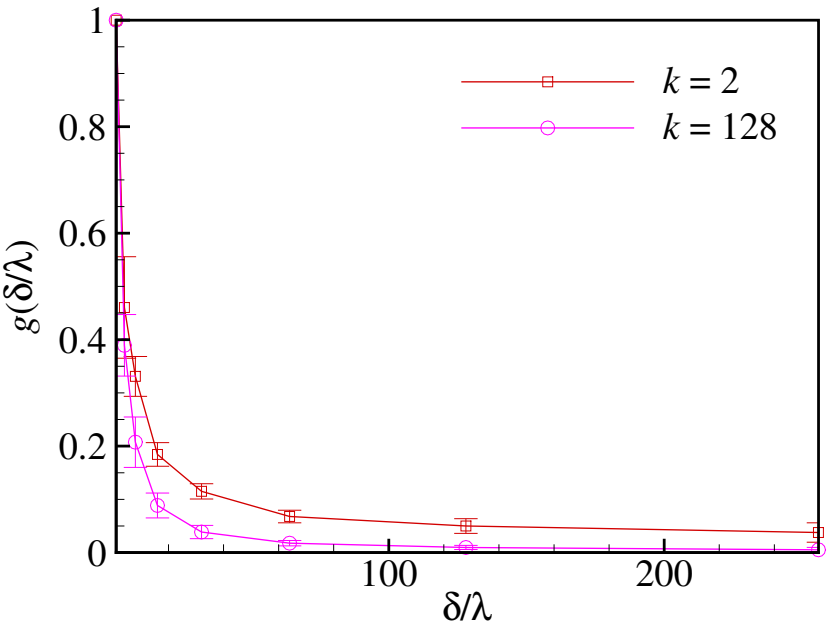

Figure 3.10: Normalized scaling function $g(\delta, \lambda)$ plotted against δ/λ for phase contrasts ($k = 2, 128$).

We need to reformulate the normalized scaling function to remove the dependence on k. The normalized scaling function $g(\delta/\lambda, k)$ can be adequately fitted with a power-law of the form[2]

$$g(\delta/\lambda, k) = \alpha(\delta/\lambda)^{-b(k)} \tag{3.23}$$

where $\alpha = 1$ as $g(\delta/\lambda, k) = 1$ for $\delta/\lambda = 1$ and $b(k)$ is the exponent that depends on k. The $b(k)$ values obtained using the power-law fit according to equation (3.23) are plotted against k in Fig. 3.11. The fit shown in the same figure is obtained according to the following equation

$$b(k) = a(k-1)^b + c \tag{3.24}$$

where a, b and c are the fitting constants. The values of the fitting constants are estimated from the fit as $a = 0.10 \pm 0.02$, $b = 0.29 \pm 0.04$ and $c = 0.50 \pm 0.01$. In the inset of Fig. 3.11, $b(k) - c$ is plotted against $(k-1)$ on a double log scale which is observed to follow a straight line with the slope $b = 0.29$ and intercept of $\ln(a) = -2.27$ giving $a = 0.10$, confirming the fit.

[2]Prepared by Sohan Kale

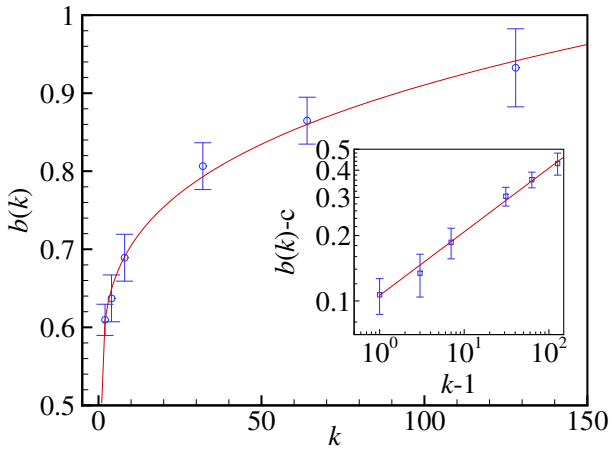

Figure 3.11: The exponent $b(k)$ from equation (3.23) plotted as a function of k with the corresponding best fit obtained using equation (3.24). (Inset) The fit is confirmed by plotting $b(k) - c$ against $(k-1)$ on a double log scale to get a straight line with the slope $b = 0.29$

Based on the equation (3.23), the reformulated normalized scaling function $h(\delta/\lambda)$ can be given as,

$$h(\delta/\lambda) = g(\delta/\lambda)\left(\frac{\delta}{\lambda}\right)^{a(k-1)^b} = \left(\frac{\delta}{\lambda}\right)^{-c}. \tag{3.25}$$

The $h(\delta/\lambda)$ obtained for $k = 2, 4, 8, 32, 64, 128$ is plotted in Fig. 3.12 showing a good collapse of the data according to equation (3.25) following the power law scaling of the form $(\delta/\lambda)^{-c}$ with $c = 0.5$ (dotted black line in the same figure).

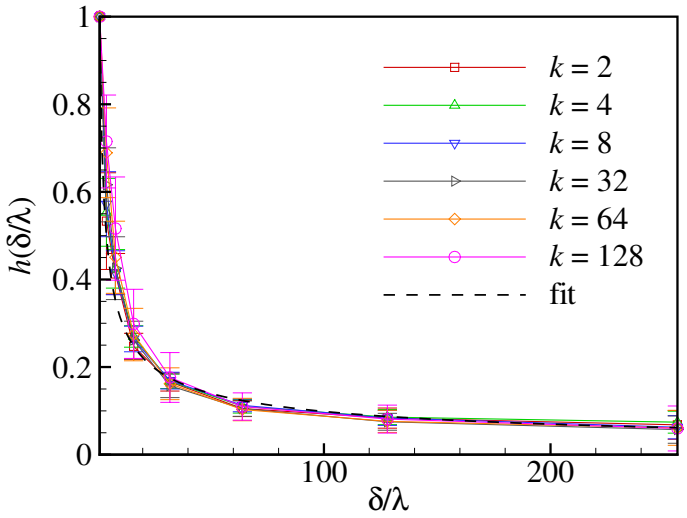

Figure 3.12: The reformulated normalized scaling function $h(\delta/\lambda)$ plotted against δ/λ for $k = \{2, 4, 8, 32, 64, 128\}$ and $\lambda = 1$. The curves collapse well following a power-law scaling of the form $(\delta/\lambda)^{-c}$ with $c = 0.5$, plotted as a dotted black line.

Thus, $h(\delta/\lambda)$ completely describes the SVE-RVE transition for a given two-phase microstructure characterized by λ and k. However, this scaling function is applicable only for nominal volume fraction of 50%. The scaling function proposed in equation (3.25) is just the special case of $h(\delta/\lambda)$ at 50% volume fraction.

A. Saharan, S. Kale, S. Koric, and M. Ostoja-Starzewski, "Homogenization of elastic responses of two-phase random microstructures with Gaussian correlations," manuscript in preparation, 2014.

Chapter 4

Fractals

4.1 Introduction

As is well known, there are numerous interpretations of fractals in the literature. Fractals have been found to accurately represent randomness combined with roughness at many scales widely encountered in nature, in effect, resulting in books with provocative titles such as *"Fractals Everywhere"* [6]. Quoting Mandelbrot [29], *"A fractal is a shape made of parts similar to the whole in some way"*, where *"some"* typically stands for "statistical". Figure 4.1 shows an example of fractal in nature. As can be observed from the Fig. 4.1, the fern leaf is made of copies of itself on smaller scales.

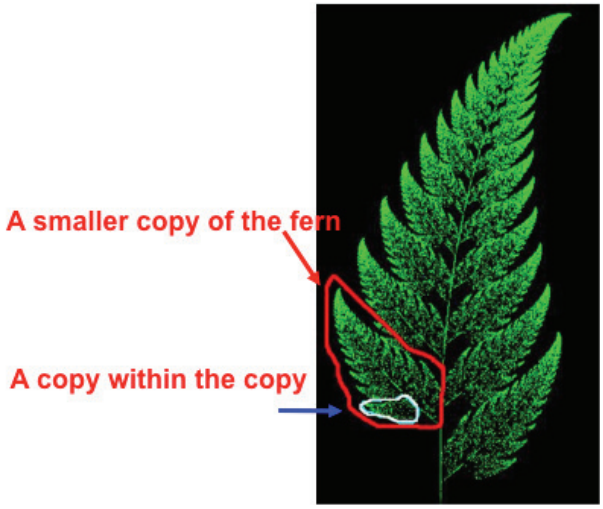

Figure 4.1: Fern leaf

Figure 4.2 shows a *Koch snowflake*, which is a mathematical fractal. As can be seen from the Fig. 4.2, a *motif* (smaller triangle), is introduced on each side of the triangle by replacing *one-third* of each of the sides at the middle at every iterative step. As a result of 20 successful iterations, one obtains a geometrical structure similar to a snowflake.

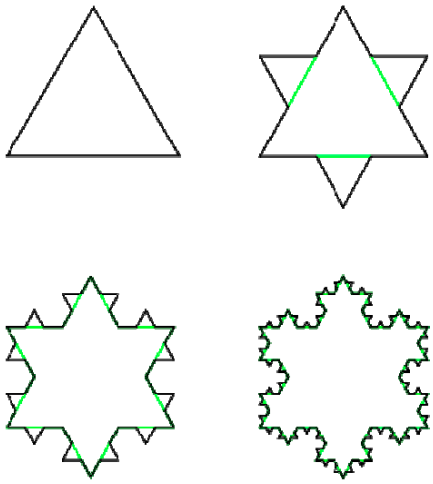

Figure 4.2: Koch snowflake

It can be seen from the Fig. 4.2, the structure is *self-similar* at every scale which can be attributed to fractals. Quoting Mandelbrot [29], *"Clouds are not spheres, mountains are not cones, coastlines are not circles, and bark is not smooth, nor does lightning travel in a straight line"*. Hence shapes and structures observed in nature are better described by fractals than by traditional euclidean shapes like rectangles, circles, spheres etc.

4.2 Fractal dimension

From an engineering point of view, it becomes essential to quantify fractals in terms of *'fractal dimension'*. Fractal dimension is routinely characterized by a power law given by the following relation,

$$N \propto r^{-D} \tag{4.1}$$

Where, N is defined as the number of a unit measure, r is the scaling factor, and D is the fractal dimension. To better illustrate the concept of fractal dimension we apply the equation (4.1) to traditional euclidean geometries to check if we can recover the topological dimension of those regular shapes (see Fig. 4.3).

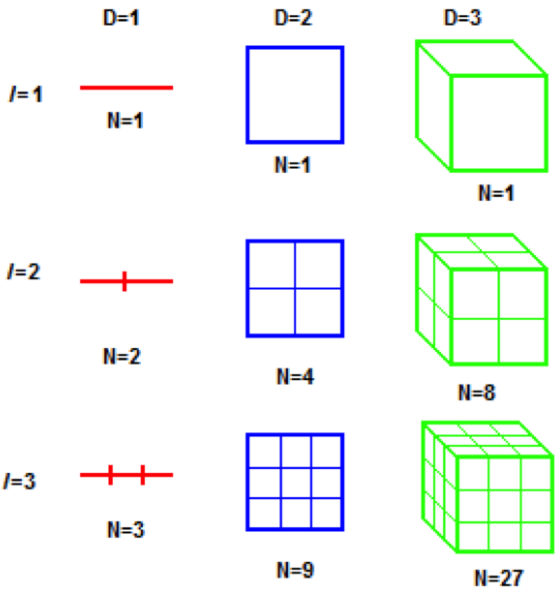

Figure 4.3: Fractal dimension equivalent to topological dimension using equation (4.1), for regular geometries

Using Fig. 4.3, for the case of a straight line segment, which is a one dimensional geometrical shape, we obtain a fractal dimension (D) of 1 using equation (4.1) as we have, $N = 3$, $r = 1/3$. Using the same equation, we obtain $D = 2$ for a square which is a 2d geometrical shape, and $D = 3$ for a cube which is a regular 3d geometry.

Using the same concept, the *'Koch snowflake'* (see Fig. 4.2) has a fractal dimension of 1.2619, as $N = 4$, $r = 1/3$. It can be inferred from this result that the *'Koch snowflake'* cannot be described by traditional euclidean geometry as it is partially plane filling, having a fractal dimension between one and two.

4.2.1 Box counting method

The box counting method is a widely used technique to measure fractal dimension. Mandelbrot [30] used this technique to measure the fractal dimension of the coast of Great Britain. The Minkowski-Bouligand dimension, also known as the Minkowski dimension or box-counting dimension, is a way of determining the fractal dimension of a set S in a Euclidean space $\mathbb{R}^n$. To calculate this dimension for a fractal S, we place this S on an evenly spaced grid and count the number of grid boxes it takes to cover this fractal set. The box counting dimension is calculated by seeing how the number of boxes to cover the fractal set is changed as the grid is made finer (see Fig. 4.4).

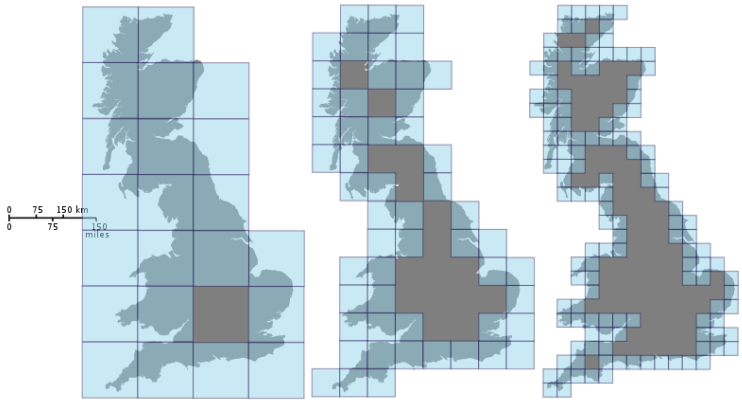

Figure 4.4: Box counting dimension for the coast of Great Britain [43]

Suppose $N(\epsilon)$ is the number of boxes of length scale ϵ required to cover the fractal set, then the box counting dimension (D) is given by the following relation,

$$D = \lim_{\epsilon \to 0} \frac{logN(\epsilon)}{log(1/\epsilon)} \tag{4.2}$$

The coasts of landmasses are highly involved curves, and have a property of *'self-similarity'* in statistical sense *i.e.* each of their portion is a smaller scale image of the whole part. Measurement of the coastlines are not trivial, and a lot depends on the length scale of the yard stick used to measure the same. Theoretically the coastlines can have an infinite length scale as the yardstick length scale used to measure them goes to zero (essentially a point). Hence, quantifying the length scales of coastlines in terms of their length seems useless. Mandelbrot [30] hence analyzed the coastlines of Great Britain, Australia, land frontiers of Portugal, Germany and found them to be fractal in nature. The fractal dimension of west coast of Great Britain was found to be 1.29...

4.3 Fractals in mechanics

Overall, there has been very little research on fractals in elastic-plastic problems except for [35],[25],[26],[34]. In those papers, sets of plastic grains were found to evolve as fractals during monotonic loading of elastic/plastic microstructures.

In classical plasticity theory of homogeneous materials, the plastic deformation occurs when the stress reaches a critical (yield) value. The deterministic model is widely employed in engineering applications due to its simplicity and accuracy. Figure 4.5 shows elastic-plastic transitions in homogeneous and random heterogeneous material models. It is clear that, under uniform boundary conditions, a homogeneous body

displays an instant transition from elastic (blue) to plastic (red) state, reflected by a sharp kink in the stress-strain curve. However, all natural and man-made materials always contain some spatially distributed randomness (material defects, impurities etc.), so that, under macroscopically monotonic loading, 'weaker' material grains and regions plasticize first and gradually spread throughout the whole material. As a result, the stress-strain curve displays a smooth transition from the elastic to plastic regime, which is physically more plausible. We are interested in the evolution of the plasticity of the material and in checking whether the evolution is fractal in nature, and can we measure the fractal dimension of the same.

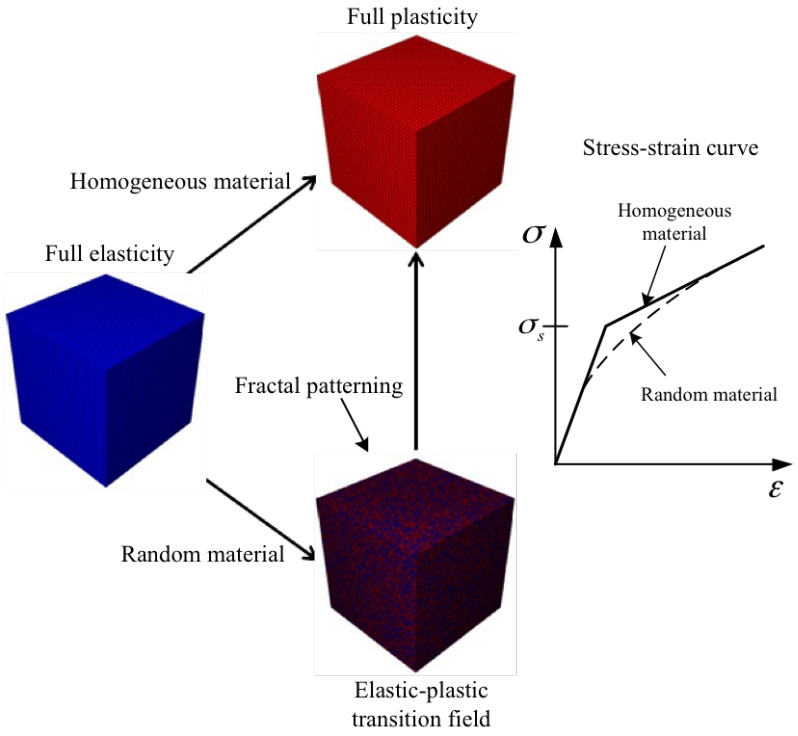

Figure 4.5: Illustration of elastic-plastic transitions in a homogeneous material versus that in a realistic, random heterogeneous material model

Previously, de Campos *et al.* [13] studied fractal behavior of the fracture stretch zone under elastic plastic conditions; it was concluded in their research that fractal description is limited for plane stress conditions. In effect, the fractal dimension can be a very good indicator of the stress and the plastic state of the material. In a related study, Herrmann *et al.* [18] estimated the fractal dimension of plastic shear bands in rocks to be ~ 1.8, and showed that from these patterns one can deduce the states of stress and deformation. Poliakov *et al.* [42] also showed that plastic shear bands in elasto-plastic materials were fractal in nature and attempted to study them using explicit techniques. Fractal patterns have also been found in failure of materials and several fracture theories accounting for such have been developed (see [4], [5], [7]).

4.3.1 Fractals in 3d[1]

A study was also carried out for elastic-plastic hardening of homogeneous materials. A 3d FEA mesh was constructed using homogeneous 316 Steel grains having uniform random scatter of up to ±2.5% in the yield stress of each of the grains. The size of the mesh was $100 \times 100 \times 100$. After applying the shear loading, fractal patterns were observed for evolving set of plastic grains, and the respective fractal dimension was calculated using the box-counting method.

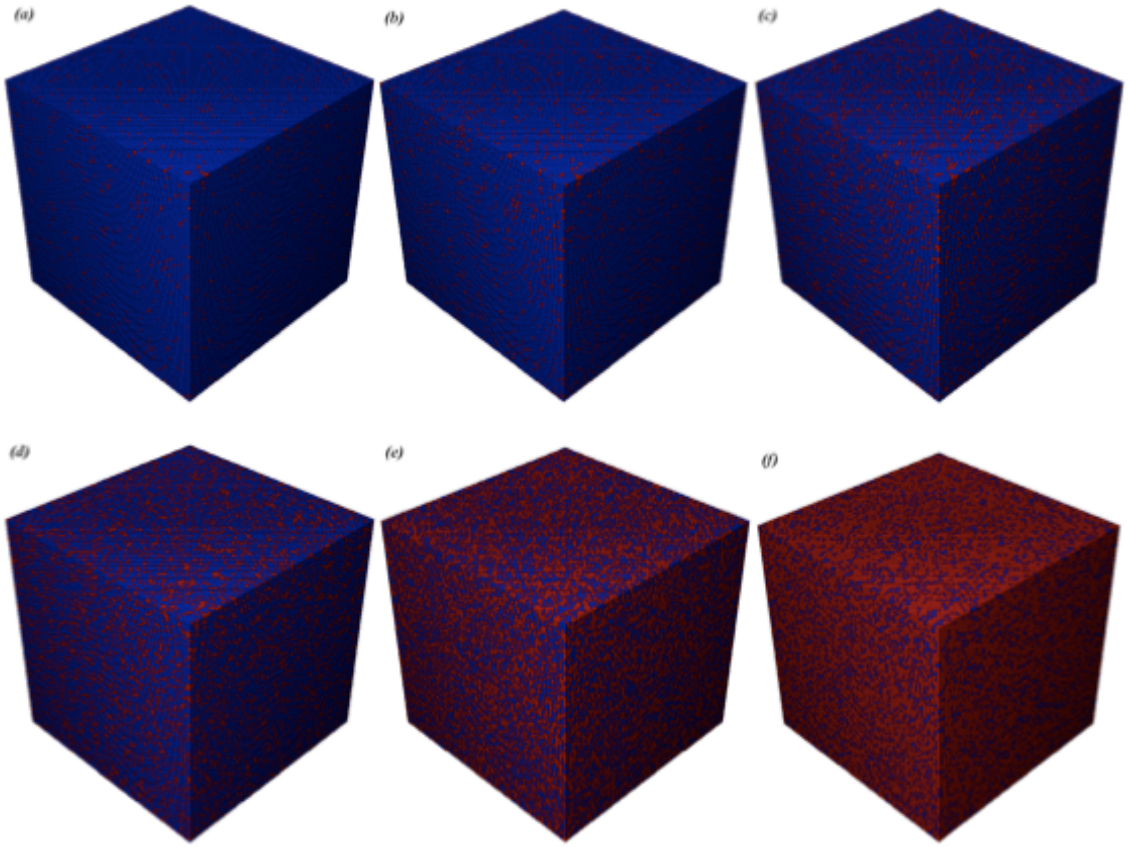

Figure 4.6: Evolution of plastic grains (red grains) in the microstructure at different load levels under displacement boundary conditions. The plastic volume fractions are: (a)5.14%, (b)8.65%, (c)15.86%, (d)27.73%, (e) 55.70%, (f)70.62%

Figure 4.6 shows the evolution of plastic grains in the microstructure. The grains are blue when they are in elastic state, and they turn red once they hit the yield limit to enter plastic state. As we can see the transition of the material from elastic to plastic is not sudden, but a smooth transition from elastic to plastic state (see Fig. 4.5). This transition is found to be fractal in nature, and the associated fractal dimensions are listed in Table 4.1.

[1] [27]

Field images	**Fractal dimension**	**Correlation coeffecient**
Figure 4.6(a)	2.696	0.9930
Figure 4.6(b)	2.778	0.9962
Figure 4.6(c)	2.918	0.9995
Figure 4.6(d)	2.977	0.9999
Figure 4.6(e)	2.992	1.0000
Figure 4.6(f)	2.999	1.0000

Table 4.1: Fractal dimension using box-counting method under displacement boundary condition

The correlation coefficients for fractal dimension for all field images are ~ 1, hence the evolution of plasticity is fractal in nature.

The fractal nature of plastic evolution in non-homogeneous materials like functionally graded materials are also found to be fractal in nature, and are discussed in detail in Chapter 5.

Chapter 5

Functionally Graded Materials

The nature abounds in heterogeneous material systems; think of wood, bone, nacre, and bamboo to name a few. Man-made examples of heterogeneous material systems include particulate composites, fiber reinforced composites, concrete to name a few. These systems offer a wider scope of application with their generally superior mechanical, thermal or electrical material properties. Or, in other words, they fill the gap in scope which single-phase homogeneous material systems leave.

The FGM is a kind of material system in which the properties and/or composition of the structure change quasi-continuously across the material domain. The basic unit of FGM is referred as a unit element. The unit element in itself would represent the local composition, microstructure, and physical configuration of the FGM. Simplest of the FGM models in two different configurations can be illustrated in the Fig. 5.1. Figure 5.1(a) represents a so-called continuous gradation from one phase to another, and Fig. 5.1(b) represents discontinuous or stepwise gradation from one phase to another [32]. Of course, the difference between these gradations hinges on how fine or how coarse the microstructure actually is.

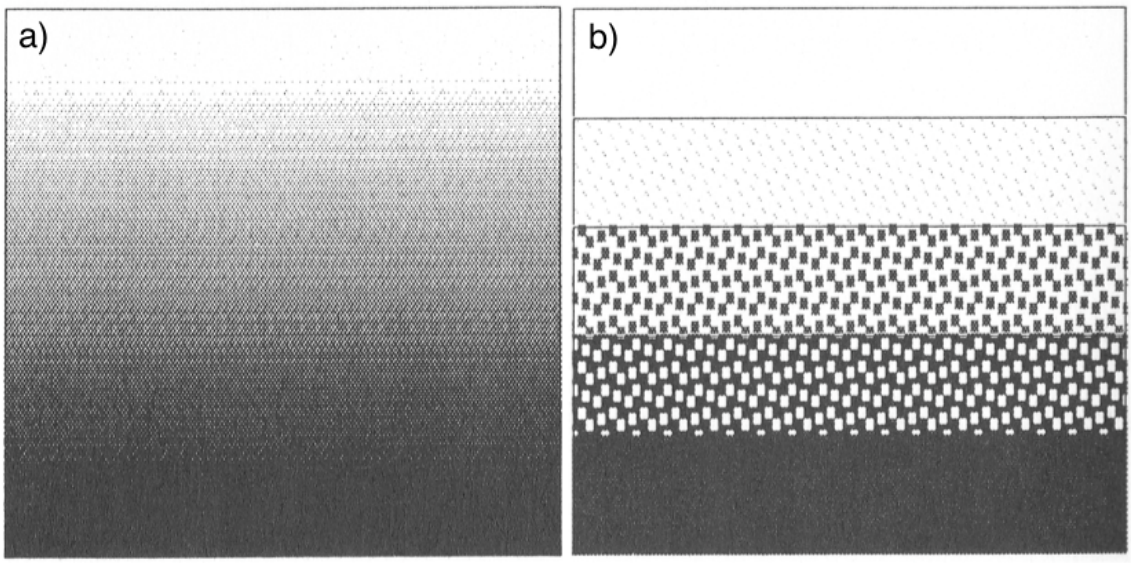

Figure 5.1: (a) Continuous gradation, (b) step-wise gradation [32]

The continuous gradation is further illustrated in Fig. 5.2(a), where the composition varies linearly as

a function of distance along in the spatial solid. Figure 5.2(b) represents how the composition changes in steps as a function of distance along in the spatial solid resulting in a layered microstructure of the FGM system.

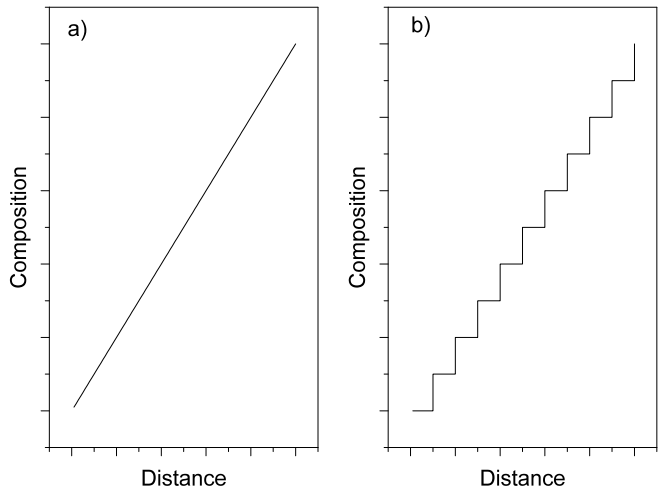

Figure 5.2: (a) Continuously graded microstructure, (b) layered microstructure

Various kinds of FGM material systems have been studied in the literature. Natural materials like bamboo have been modeled as FGM material systems [53]. Anandakumar *et al.* [3] studied thermal stress and failure analysis in functionally graded solid oxide fuel cells. Gunes and Aydin [16] studied elastic response of graded material system containing Metal (Al) and Ceramic (SiC) phases. The studies on FGM have been carried out in both the two-dimensional (2d) and 3d models, and for various loading cases including dynamic loading, low velocity impact loading, static elastic response, elastic-plastic transitions. Reliability analyses of FGM with random constitutive mechanical properties have resulted in a non-linear power-law distribution of mechanical properties. The probabilistic-based reliability analyses were performed using Monte Carlo simulations, and mechanical properties distributions were estimated using Galerkin Finite Element and Newmark Finite Difference methods [20].

The material system considered here is Ti-TiB (metal-ceramic). This material system has tremendous scope in armor-ballistic applications, as TiB, a ceramic can sustain damage from high velocity projectiles. The other phase, Titanium, being a softer material may serve as a containment unit [38]. Another application of this system is in the automobile industry. The exhaust valve of automobiles made from this material system has exhibited enhanced durability and reliability [52]. Yet another possible application of this system is the heat shields of space vehicles. During the reentry into the earth's atmosphere, surfaces of these shields

are exposed to massive amounts of friction with the earth's atmosphere leading to significant heating of the exposed surface. Conventionally ceramic tiles are used for protection as these materials provide excellent heat protection, though at some weight penalty. As a stepping-stone in this direction, in this study we research such an FGM system, as the TiB phase, just like any ceramic, would provide excellent heat shielding while the Titanium phase would reduce the weight cost while maintaining the structural integrity.

5.1 Model formulation

The FGM microstructure is modeled on a random checkerboard model as mentioned in §2.1. The indicator function is assumed to have a linear dependence in x (see Fig. 5.3(a)). Figure 5.3(b) gives an example of one realization, $\mathcal{B}(\omega)$ at $\delta = 200$.

$$P\{\chi(x)\} = x/L, \qquad x \in [0, L] \tag{5.1}$$

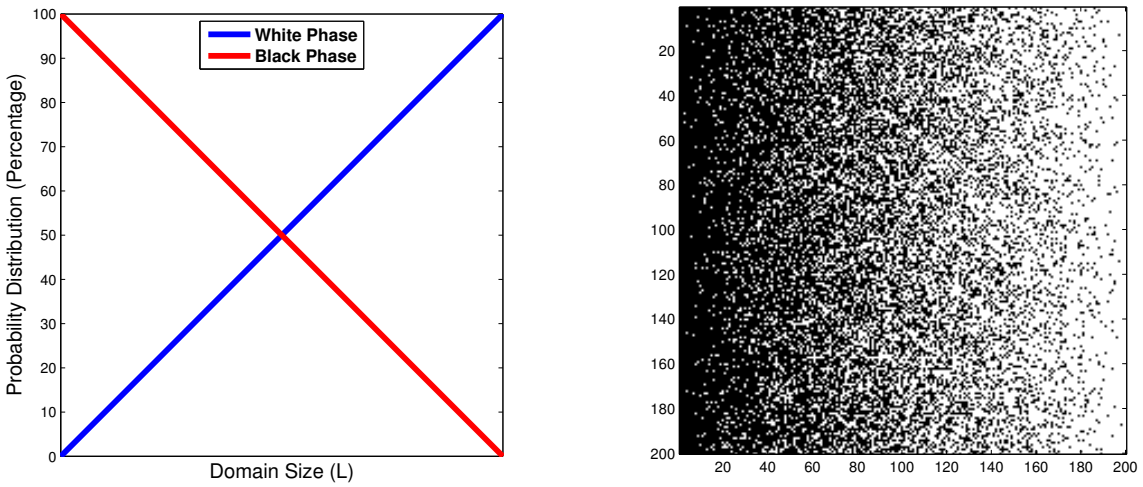

(a) (b)

Figure 5.3: (a) probability of black and white material phases in function of position across the FGM, (b) One realization of FGM microstructure

Of course, the indicator function gives the micro-scale (local) property at any point

$$C(\omega, x) = \chi_{white}(\omega, x)C^{white} + [1 - \chi_{black}(\omega, x)]C^{black} \tag{5.2}$$

but the micromechanics will be used subsequently to determine the effective properties of FGM.

At this point, fineness (δ, mesoscale or domain size) is defined as the number of grains of either phase

across the FGM; the higher the fineness, the lower the actual number describing it. Figures 5.5(a), and 5.5(c) gives examples of $\mathcal{B}(\omega)$ at different fineness levels within the same size domain.

The system to simulate the model at hand as stated earlier is a metal-ceramic system (Titanium-Titanium Monoboride, see figure Fig. 5.4). This material system allows us to examine the graded microstructure with large contrast between the two phases, with the ceramic phase a lot harder than the metallic one. In essence the constitutive response of the FGM system will be an intermediate between the Titanium and Titanium Monoboride phases (see Fig. 5.7).

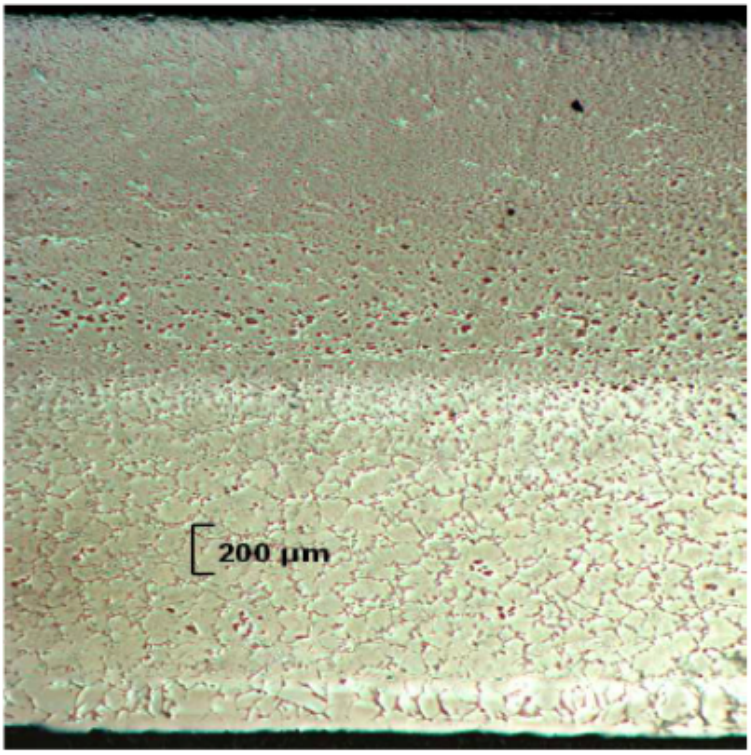

Figure 5.4: Microscopic view of Ti-TiB FGM. Ti region near the top; TiB region near the bottom [24]

Sections §5.2, and §5.3 provide the background for new results reported in sections §5.4, and §5.5 (taken from my M.S. thesis at UIUC [51], see also [50]).

5.2 Interfacial fractal dimension

Furthermore, we are interested in the interface edges between the black and white phases, which leads us to introduce so-called edge plots (Fig. 5.5). Since these interface edges appear in a disordered fashion throughout the domain, we observe dense edge structures in the middle of the domain, as that is the place where the coexistence of black and white phases (or their mixing) is the highest with $P(black, white) =$

$\{0.5, 0.5\}$, i.e. the probability distribution of each phase.

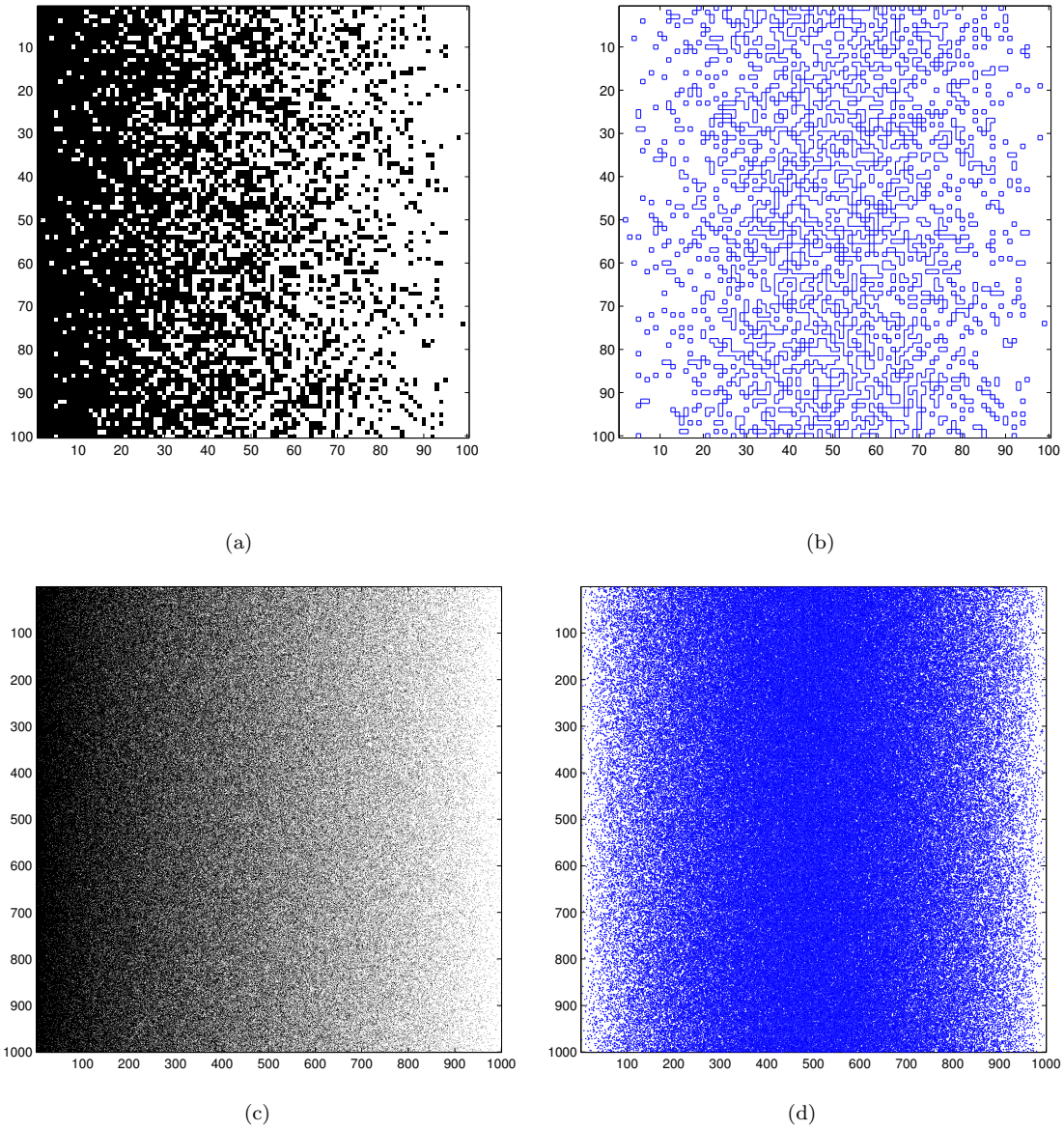

Figure 5.5: (a) FGM microstructure at fineness of 100, (b) Edge plots corresponding to fineness of 100, (c) FGM microstructure at fineness of 1000, (d) Edge plots corresponding to fineness of 1000

Although the probability distribution of either phase is varying linearly across the material domain, the FGM has a fine structure at smaller scales down to the grain level, and is too irregular to be easily described by the traditional Euclidean geometric language. We focus on the black-white interfaces, henceforth referred to as an edge set. In other words, neither the white-white nor the black-black interfaces contribute to the edge set. Now, we measure the fractal dimension D (equation (5.3)) of these edges on various levels of

fineness (domain size), and study the variation in the fractal dimension across the solid.

$$D = \frac{Log_{10}(R)}{Log_{10}(N)} \tag{5.3}$$

Here R represents the number of the edges in the domain, N represents the domain size, and D represents the corresponding fractal dimension. For example, for one simulation of domain size = 10, we find D = 1.4548. We call this the *interfacial fractal dimension*.

Of course, since domain size=10 is too small a scale to reliably discuss fractals, we see a strong noise-to-signal ratio in the estimation of D (Fig. 5.6). However, as we go to finer systems we observe that this noise decreases and the fractal dimension stabilizes between 1.765 and 1.75. For domain size=1,000, D further stabilizes (over 100 simulations) at 1.84, and for domain size=10,000 (over 100 simulations), it attains approximately$\sim$1.88.

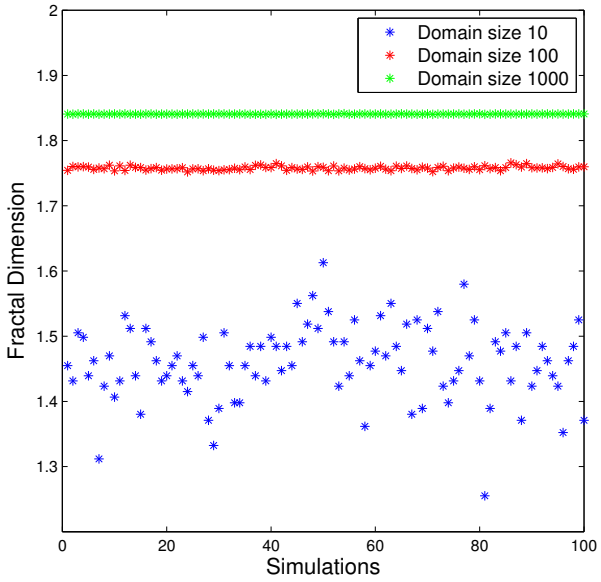

Figure 5.6: Fractal dimension for varying domain sizes (δ)

Now, we further look at how this interfacial fractal dimension is varying lengthwise and widthwise across the solid. For the sake of characterizing and observing the distribution of the interfacial fractal dimension as we move on, we consider a scale of 1,000. The interfacial fractal dimension is estimated locally using the equation (5.3) described earlier in this section. The edges or interfaces are counted locally as a function of their position as we move across the solid both lengthwise and widthwise. Figure 5.7 shows how this interfacial fractal dimension is varying across the system.

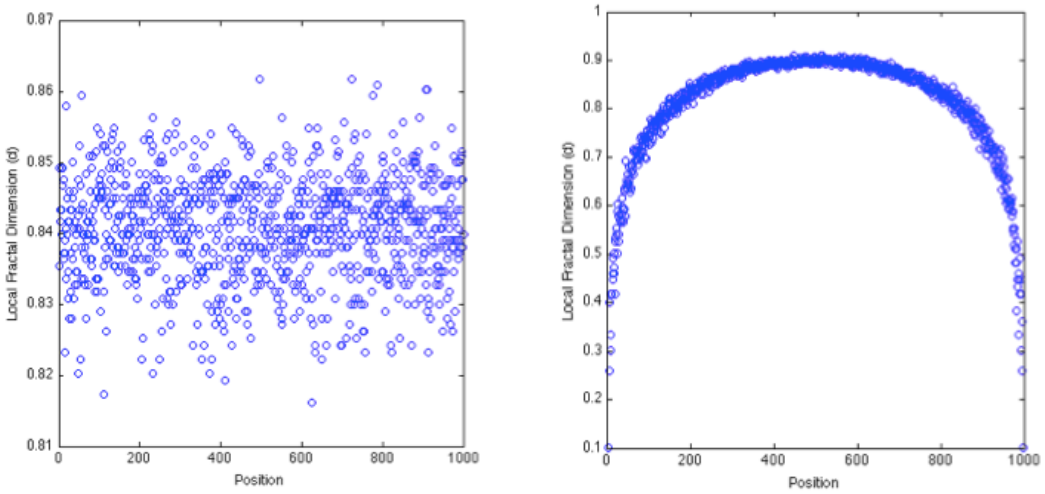

(a) (b)

Figure 5.7: (a) Variation in local interfacial fractal dimension widthwise (top-bottom), (b) Variation in local interfacial fractal dimension lengthwise (left-right)

It is evident from Fig. 5.7(a) that the variation in local fractal dimension does not show any trend as we move though the solid widthwise. However, a clear trend can be discerned from Fig. 5.7(b), where the variation in local fractal dimension is plotted as a function of position in the solid. We now go ahead and characterize this trend by curve fitting. The Fourier fit and Beta function fit were applied to characterize this trend.

The Fourier fit was applied using MATLAB curve fit toolkit and the results are given in Fig. 5.8.

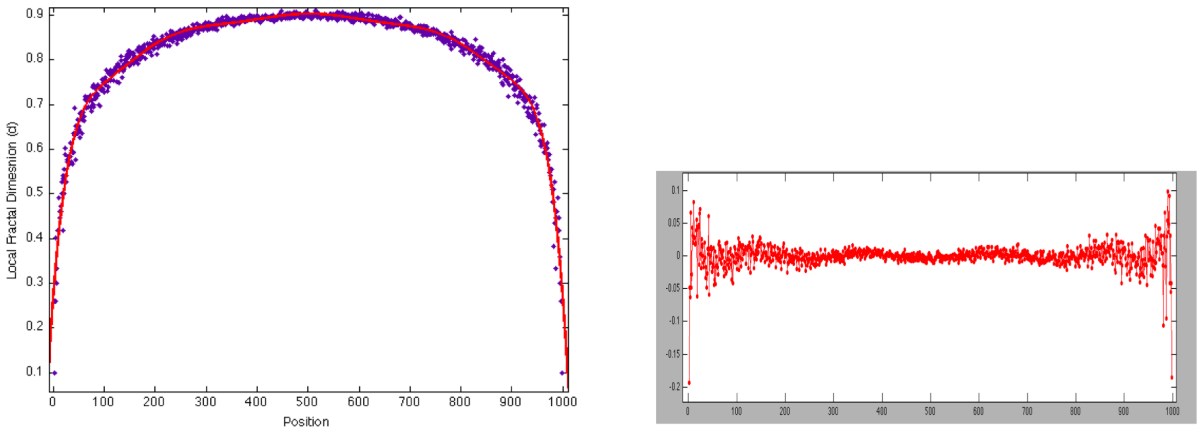

(a) (b)

Figure 5.8: (a) Fourier fit (red line) applied to the local fractal dimension, (b) Fourier fit residuals

The red line on the plot in the Fig. 5.8(a) represents the fit. The equation for the fit is given by the

following equation,

$$f(x) = a_0 + a_1 cos(\omega x) + b_1 sin(\omega x) + a_2 cos(2\omega x) + b_2 sin(2\omega x) + a_3 cos(3\omega x) + b_3 sin(3\omega x) \\ + a_4 cos(4\omega x) + b_4 sin(4\omega x) + a_5 cos(5\omega x) + b_5 sin(5\omega x) \tag{5.4}$$

The values of the coefficients of the Fourier fit are as follows:

$$\begin{aligned} a_0 &= -3.897e+06; \omega = 0.2666 \\ a_1 &= 6.525e+06; b_1 = -1833 \\ a_2 &= -3.781e+06; b_2 = 2098 \\ a_3 &= 1.451e+06; b_3 = -1182 \\ a_4 &= -3.331e+05; b_4 = 350.5 \\ a_5 &= 3.473e+04; b_5 = -43.7 \end{aligned} \tag{5.5}$$

Another fit is applied to the trend observed in Fig. 5.7(b) using the *Beta* function [10], see the solid red line in Fig. 5.9(a). The corresponding residuals are plotted in Fig. 5.9(b). The beta function $B(x, y)$ is given by the following relation,

$$B(x, y) = \frac{\Gamma(x)\Gamma(y)}{\Gamma(x + y)} = \int_0^1 t^{x-1}(1 - t)^{y-1} \mathrm{d}t \tag{5.6}$$

$\Gamma(z)$ is called the gamma function given by,

$$\Gamma(z) = \int_0^\infty t^{z-1} \mathrm{e}^{-t} \mathrm{d}t \tag{5.7}$$

The equation representing the fit given in Fig. 5.9(a) is given by,

$$f(x) = \frac{x^{\alpha-1}(1 - x)^{\beta-1}}{B(\alpha, \beta)} C \tag{5.8}$$

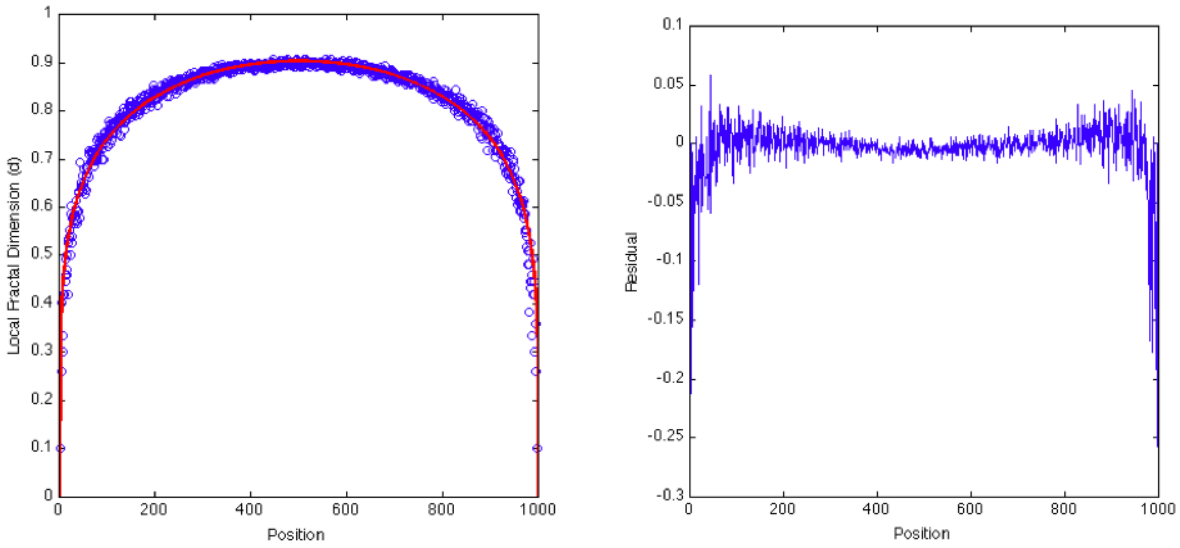

(a) (b)

Figure 5.9: (a) The beta function fit (red line) applied to the local fractal dimension, (b) beta function fit residuals

Where α, and β equal 1.692, and $C = 0.8129$. The equation (5.8) represents a much simpler function, and a fit that is easier to represent than that of equation (5.4). The residual plot in Fig. 5.9(b) also shows considerable noise in the residuals at the boundaries, which is analogous to the residual behavior of the Fourier fit given in Fig. 5.8(b).

5.3 Fractal characterization of elastic-plastic transitions in 2d FGM

Our decision to involve fractals in combination with scale-dependent homogenization is also supported by a review of many studies (see [1]) of mechanical responses of FGMs. Aboudi *et al.* [1] while studying the thermoplastic response of an FGM, concluded that conventional homogenization suffered from clear drawbacks. Concerning the mechanics, we investigate the response of the entire FGM (Ti-TiB) domain under the UKBC and USBC (equations (1.6) and (1.7)) as they will provide bounds on the overall constitutive behavior.

Titanium being a softer material, it undergoes plastic deformation, and the TiB being a ceramic, remains elastic throughout. However, the spatial patterns associated with the phenomenon seem to be unknown as yet. Overall, the response of FGM made of Titanium-TiB is expected to have an intermediate response between its two constituent phases as shown in Fig. 5.10.

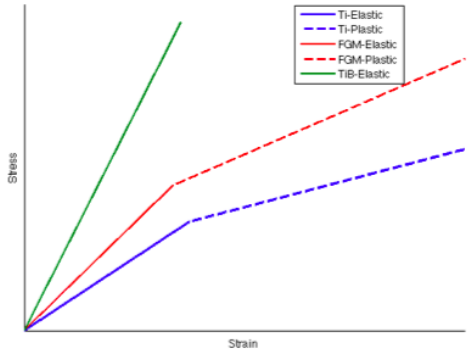

Figure 5.10: Illustration of stress-strain response of the Ti-TiB FGM and it's two constituent phases

Essentially, Titanium is an anisotropic material. It is a hexagonal closed packed (HCP) crystal at room temperature. TiB on the other hand is a hard brittle ceramic. The crystal structure of TiB is B27 class orthorhombic [24]. For our model constructed, we have assumed isotropic response for Titanium and TiB, with Titanium undergoing isotropic plastic hardening beyond its yield point. The material properties we have taken for Titanium is for the A70 commercially available pure titanium. Its properties are given in Table 5.1.

Properties	**Young's modulus (E) GPa**	**Poisson's ratio (ν)**	**Yield Strength (σ_0) MPa**	**Density (ρ) Kg/mm^3**
Ti	104	0.3	483	4512
TiB	370	0.4	-	4630

Table 5.1: Material parameters for commercially pure Titanium (A70) at room temperature [8, 11, 24], and TiB at room temperature [24]

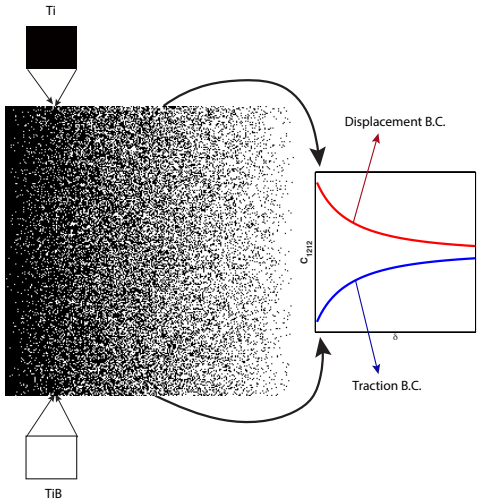

Figure 5.11: Homogenization procedure for 2d graded microstructures

The plastic deformation in A70 follows a hardening law given by the following equation [8],

$$\sigma = \sigma(0) + h\sqrt{\varepsilon} \tag{5.9}$$

Where σ is the flow stress, $\sigma(0)$ is the intercept, h is the strain hardening coefficient, and ε is the true strain. Titanium has $\sigma(0)$ of 510 MPa, and the value for h is 833 MPa [8].

Pure shear is applied using uniform kinematic and uniform static boundary conditions as given by equations (5.10),(5.11) as described in §1.2.1. The fineness scales under consideration were $50, 100$, and 200. The UKBC for pure shear is applied on the model according to,

$$\begin{aligned} u &= \varepsilon^0 \cdot x, \quad \forall x \in \mathcal{B} \\ \varepsilon^0_{11} &= \varepsilon^0_{22} = 0 \\ \varepsilon^0_{12} &= \varepsilon^0_{21} = \varepsilon \end{aligned} \tag{5.10}$$

The USBC for pure shear is applied on the model according to,

$$\begin{aligned} t &= \sigma^0 \cdot n, \quad \forall x \in \mathcal{B} \\ \sigma^0_{11} &= \sigma^0_{22} = 0 \\ \sigma^0_{12} &= \sigma^0_{21} = \sigma \end{aligned} \tag{5.11}$$

The load applied (traction or displacements) on the graded microstructure are refined to a degree through which elastic-plastic transitions can be analyzed. The results of the mechanical testing in 2d were plotted as volume averaged von Mises stress against a volume averaged plastic strain. This was done essentially to check if the classical RVE response of the material was achieved as we moved up our scale.

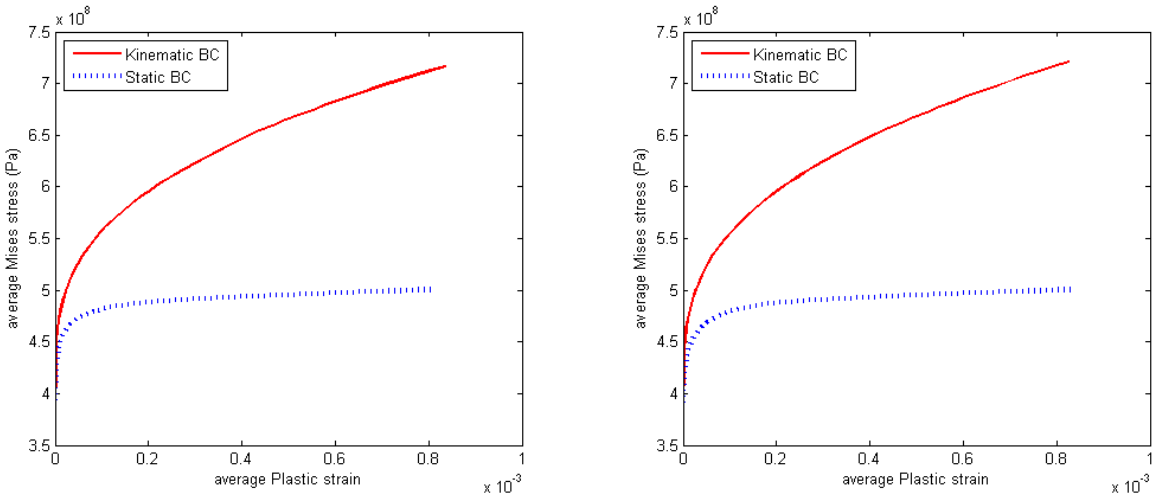

(a)

(b)

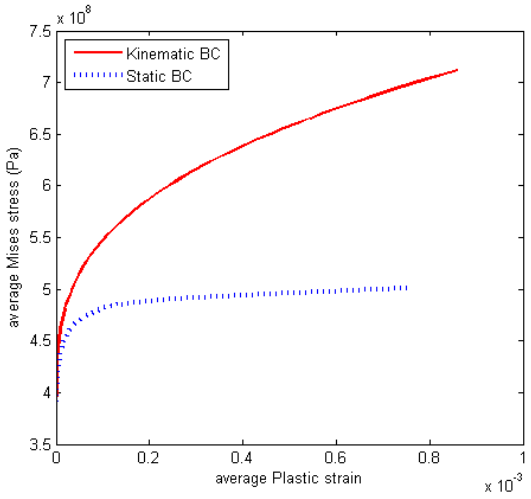

(c)

Figure 5.12: Volume averaged stress-strain response under different BC's at fineness of (a) 50, (b) 100, (c) 200

Figure 5.12 clearly shows that classical constituent RVE response of the graded microstructure is not achieved under UKBC and USBC. Even as we increase our fineness, or in other words refine our microstructure, we do not see any closing of the material response under the respective BC's. This could be reasoned out due to many reasons. Firstly, the USBC (traction) is very sensitive and often ill posed to elastic-plastic problems. Our calculations thus for plastic strain under this boundary condition in not reliable as it is underestimated due to lack of numerical efficiency of ABAQUS linear solver to account for large plastic strains. Even if we could account for large plastic strains, the response would still not match the response under UKBC (displacement). Secondly, as our material is heterogeneous, with the TiB phase remaining elastic

throughout, it does not reach high stress levels under USBC, even though the softer Ti phase continues to sustain large plastic strain due to plastic flow of the material. This indicates that out model is highly sensitive to the way it is loaded, and even a small change in loading conditions could elicit a varied response from the material.

Further the evolution of plasticity in the graded microstructure of Ti grains is studied from the viewpoint of fractals. Evolution of plastic grains at a fineness of 200 under UKBC and USBC are illustrated in Figs. 5.13 and 5.14 respectively.

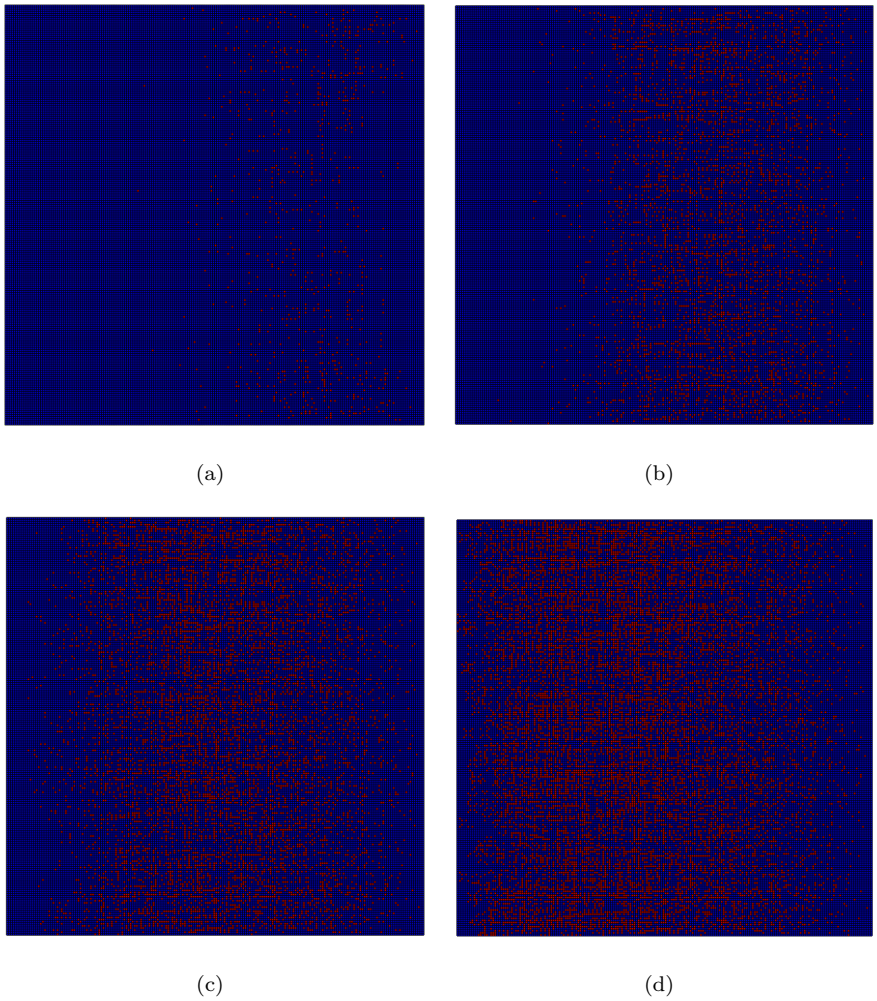

(a) (b)

(c) (d)

Figure 5.13: Evolution of plasticity (red pixels) in Ti grains under UKBC at fineness 200 at increasing load levels from (a) to (d)

Figure 5.13 shows the evolution of plasticity in the Ti grains (indicated by red pixels) under UKBC starts towards the right side of the domain, which is a TiB rich region. This is understandable as uniform displacement on TiB boundary causes extremely high stress levels in TiB rich regions leading to plastic formation of Titanium grains in that region. As we move into the loading sequence, we observe that the

plastic grains then slowly start evolving towards the Titanium rich regions on the left side of the domain.

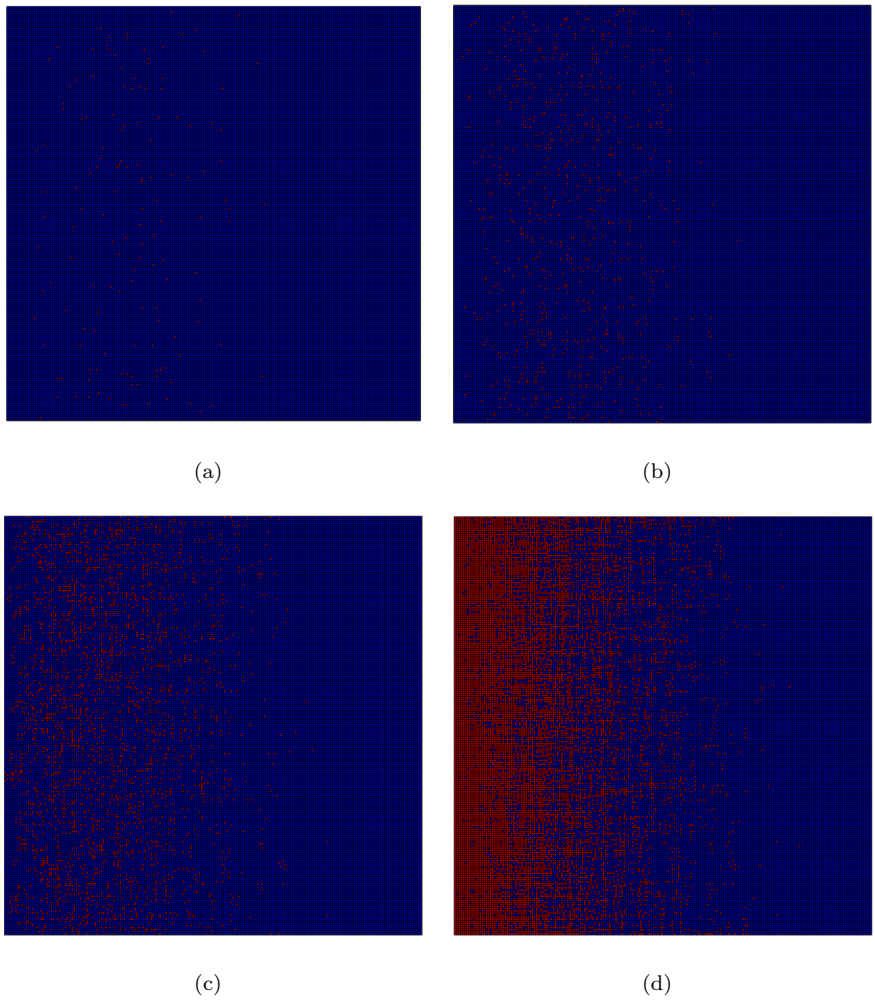

(a) (b)

(c) (d)

Figure 5.14: Evolution of plasticity (red pixels) in Ti grains under USBC at fineness 200 at increasing load levels from (a) to (d)

Now, looking at Fig. 5.14 we see the evolution of plastic grains (red pixels) growing from Titanium rich regions (from the left). This can be reasoned as, under USBC leads to high stress levels in the Titanium rich regions, which leads to plastic flow in the material leading to plastic evolution of the grains. As we proceed through the loading sequence, the plastic evolution of the Titanium grains starts progressing towards the middle of the system, with very few grains undergoing plastic deformation in the TiB region. This is because under USBC, the stress in TiB rich region doesn't reach levels high enough to cause plastic deformation of Titanium grains in the TiB rich region.

We can now estimate the fractal dimension D of the plastic grains evolving under both UKBC and USBC. It is done using the box counting method [25] (as discussed in §4.2.1) at fineness of 50, 100 and 200 at the end of the loading curve. The box counting method involves counting the number of boxes (Nr) of

a particular edge length (r) required to cover the plastic grains in the entire domain. The plastic domain taken into consideration has plastic deformation ranging from 25% to 27% (for both boundary conditions) of the total 50%, which is the maximum plastic deformation for our model.

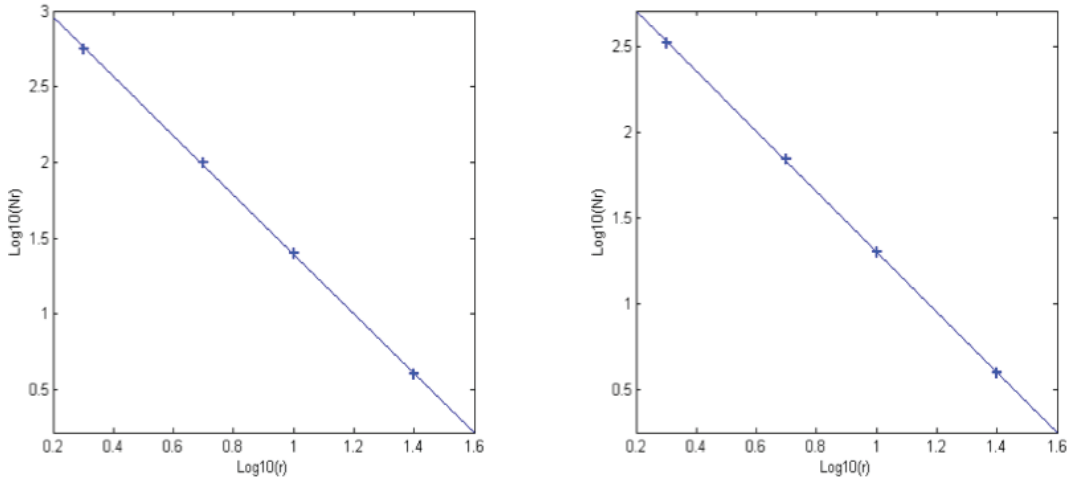

Figure 5.15: Estimation of the fractal dimension using box counting at fineness of 50 under (a) UKBC ($D = 1.9586$) and (b) USBC ($D = 1.7558$)

In Fig. 5.15 we plot the log-log relationship between the number of boxes (Nr) and the edge length of the box (r), for both the boundary conditions. The fractal dimension for the UKBC and USBC is 1.9586 and 1.7558, respectively. The correlation coefficients in both cases were found to be very close to 1. The difference in the D (fractal dimension measured using box-counting), for both boundary conditions can be attributed to the plastic evolution of grains under respective boundary conditions as illustrated in Fig. 5.13 and Fig. 5.14. Under UKBC, the plastic grains are more evenly distributed in the entire domain, and hence the higher D. For the case of USBC, the plastic grains are mainly concentrated towards the Titanium rich region on the left side of the domain, hence the lower D. This validates our result of the mechanical testing of our model, where we found that the overall material response is extremely sensitive to the loading conditions.

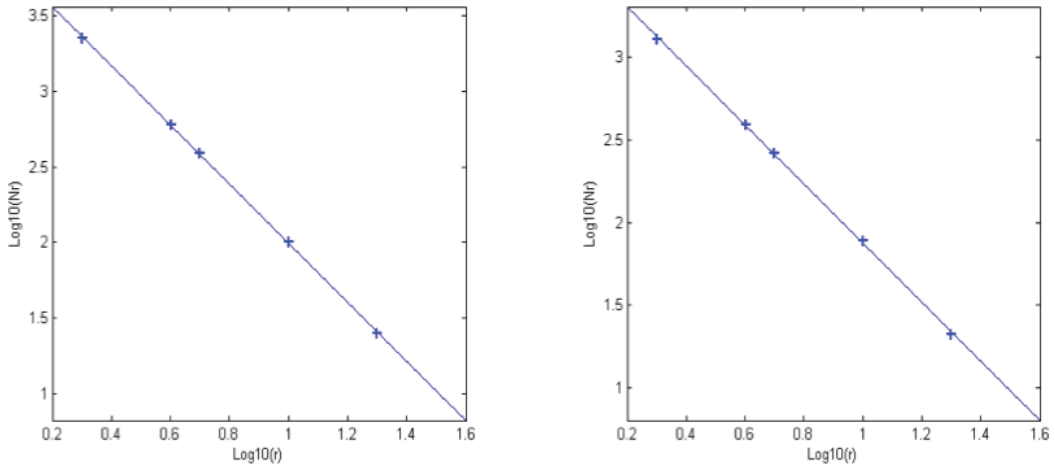

(a) (b)

Figure 5.16: Estimation of the fractal dimension using box counting at fineness of 100 under (a) UKBC ($D = 1.9555$) and (b) USBC ($D = 1.7837$)

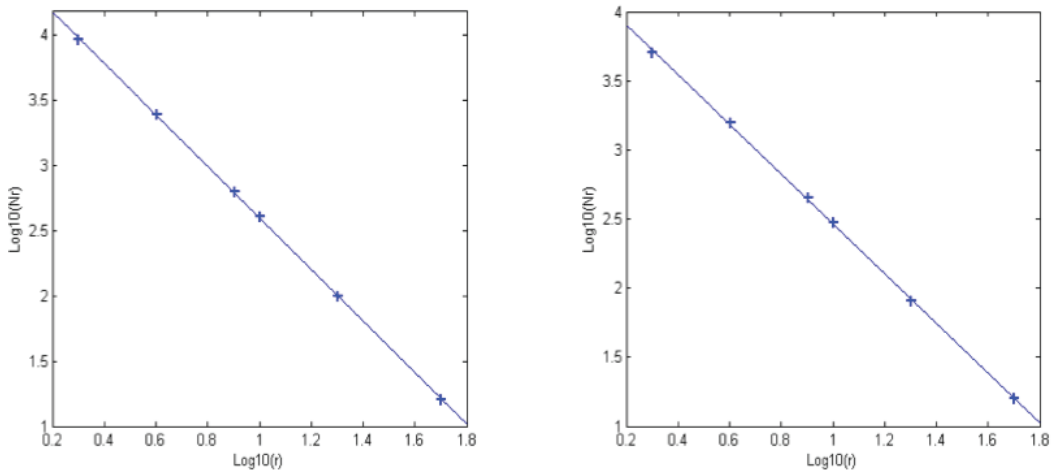

(a) (b)

Figure 5.17: Estimation of the fractal dimension using box counting at fineness of 200 under (a) UKBC ($D = 1.9739$) and (b) USBC ($D = 1.7981$)

We again plot the log-log relationship between the number of boxes (Nr) and the edge length of the box (r) at fineness of 100 and 200 in Fig. 5.16 and Fig. 5.17 respectively. The correlation coefficient as we can see from all the four plots has been estimated to be very close to 1.

The fractal dimension (D) for both the boundary conditions for all fineness scales under consideration i.e. 50, 100 and 200 show little variation among themselves, and hence D can be a very useful parameter to estimate the plastic deformation for two-phase linearly graded FGM .

5.4 Elastic homogenization of 3d Functionally graded materials

The graded microstructure is constructed in 3d by stacking graded microstructures in 2d (see §5.1) in the third dimension (*'z direction'*). Homogenization for the elastic shear response is carried out using the Hill condition (see §1.2.1).

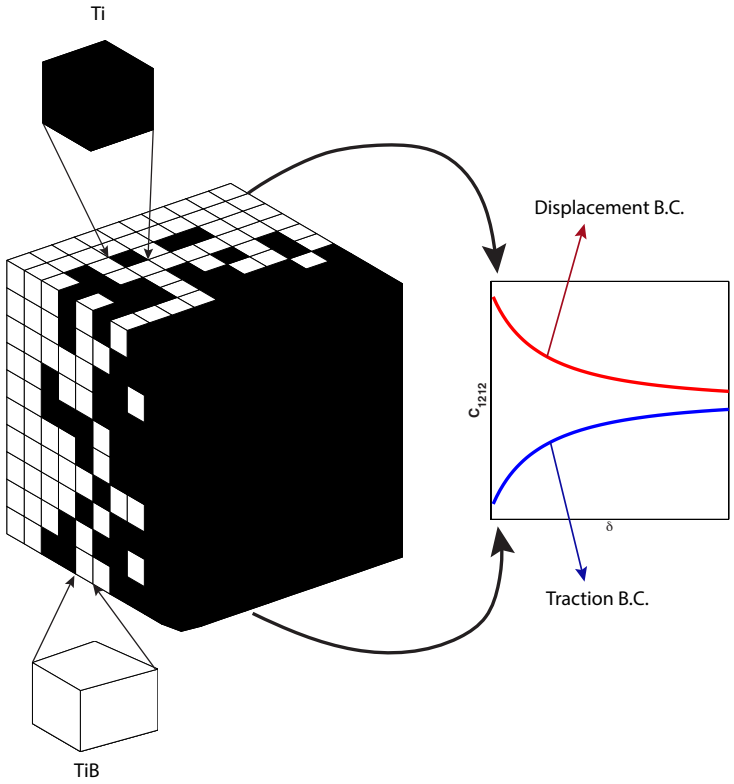

Figure 5.18: Homogenization procedure for 3d graded microstructures

Two material systems are considered here: metal ceramic system (Ti-TiB) (from §5.3), and metal - metal system (Cu-Ni). The elastic material properties are the same as those listed in Table 5.1. A few studies on 3d graded microstructures have been conducted involving wave propagation [39], and crack propagation [41, 40]. In our study we analyze the graded microstructure numerically under uniform kinematic and uniform static boundary conditions in order to uniquely characterize the constitutive response.

5.4.1 Computational procedure

The numerical analyses in 3d are carried out using finite elements on different levels of fineness, similar to the numerical analysis of graded microstructures in 2d. Like in 2d, the graded microstructure contains grains of Ti and TiB. A weaker contrast graded microstructure with Copper and Nickel is also studied. The grains are assumed to be locally isotropic in nature and perfect bonding between the grains is assumed as

well. The 3d analyses results in massive simulations performed in parallel using commercially available FEM package called Abaqus. The simulations were carried out using the computational resources available at the National Center for Supercomputing Applications (NCSA). We used *Taub* cluster under Illinois Campus Cluster program available at NCSA. For our biggest problem, we used the High Performance Computing (HPC) cluster called *iForge*. *iForge* is at the National Center for Supercomputer Applications (NCSA) and is specifically built and tuned to accelerate some of the toughest industrial HPC workflows. The current configuration consists of 144 dual socket Dell PowerEdge M620 nodes, each with two Xeon E52680 10-core CPUs, and 20 cores total, operating at 3.0 GHz, and 44 of them with 256GB of RAM. They are connected with QDR Infiniband networking fabric. We used Abaqus/Standard 6.13 implicit direct parallel solver. The large memory of iForge allowed as to keep all the factorization date in memory (in-core solver) thus significantly accelerating the solution time in addition to parallel processing. The largest problem we solved, 50^3 fineness size and 200^3 mesh size, has 8 million elements-each with different material properties, and over 24 million DOFs. Different scales of fineness are indicated in Fig. 5.19.

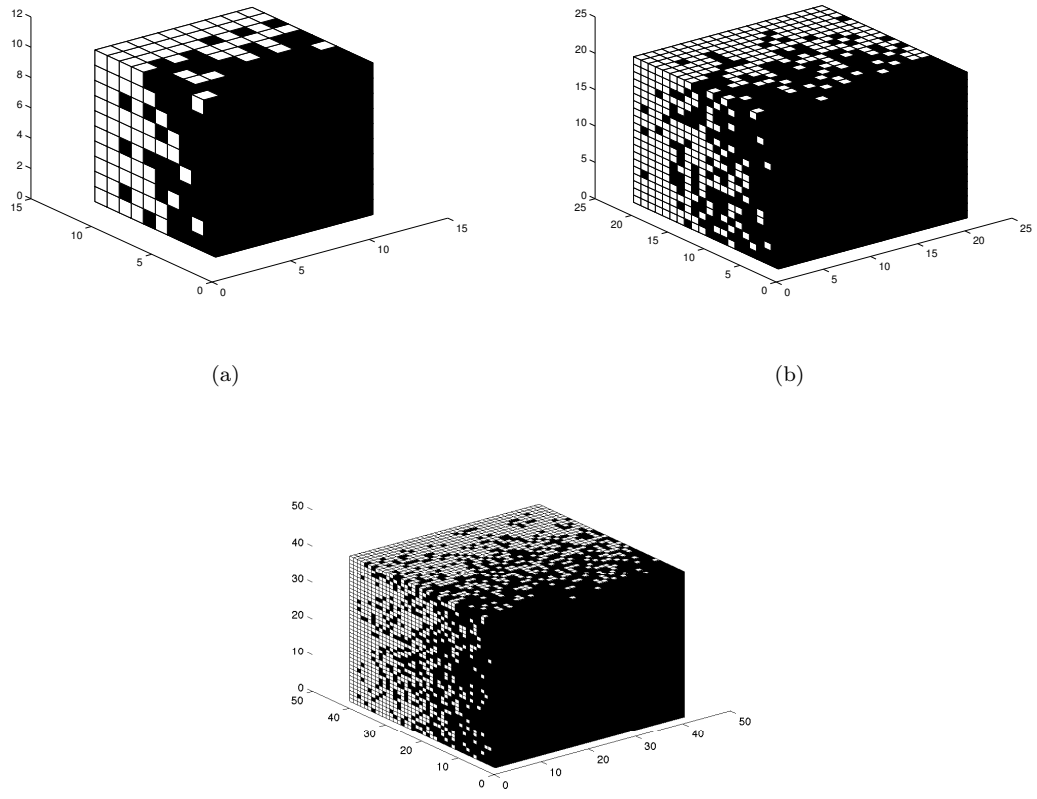

(a) (b)

(c)

Figure 5.19: 3d FGM microstructure at fineness (a) 10, (b) 20, (c) 40

The numerical analyses in 3d was carried out on various levels of fineness. The results were averaged over finite a set of realizations (N) for each level of fineness (δ) as indicated in Table 5.2.

δ	**N**	**D.O.F.**	**Cluster**	**Nodes**	**Time**
10	50	$\sim 200K$	Taub	8	$\sim 25min$
20	50	$\sim 15M$	Taub	8	$\sim 2.5hrs$
40	5	$\sim 12M$	iForge	6	$\sim 1.5hrs$
50	5	$\sim 24M$	iForge	10	$\sim 7hrs$

Table 5.2: Summary of numerical analysis listing the complexity at each level of fineness, and computational cost

The mesh density used for this set of problems was 4. This means that carrying out numerical analysis on a realization of fineness 50 resulted in solving a problem of mesh $200 \times 200 \times 200$. This was chosen to avoid the stress concentration due to high contrast in the material properties of the two phases and get accurate results. Another 3d FGM system was also studied with a weak contrast in material properties of the two phases. The system chosen is a metal-metal (Cu-Ni) FGM system. The material properties of the individual phases are listed in Table 5.3. Since the contrast between the material properties of the two phases is small, hence mesh density chosen for this material system is 2. This means that carrying out numerical analysis on a realization of fineness 50 resulted in solving a problem of mesh $100 \times 100 \times 100$.

Properties	**Young's modulus (E) GPa**	**Poisson's ratio (ν)**
Copper	122.72	0.326
Nickel	199.78	0.322

Table 5.3: Material parameters for Copper and Nickel [49]

The results of the homogenization our presented in the following section (§5.4.2), and a scaling behavior is also analyzed using equations mentioned in section §3.4.

5.4.2 Results

To homogenize the shear response of the graded microstructure, same methodology (Hill condition), is applied using equation (1.6) and (1.7). The results for the Ti-TiB graded microstructure are presented in Fig. 5.20.

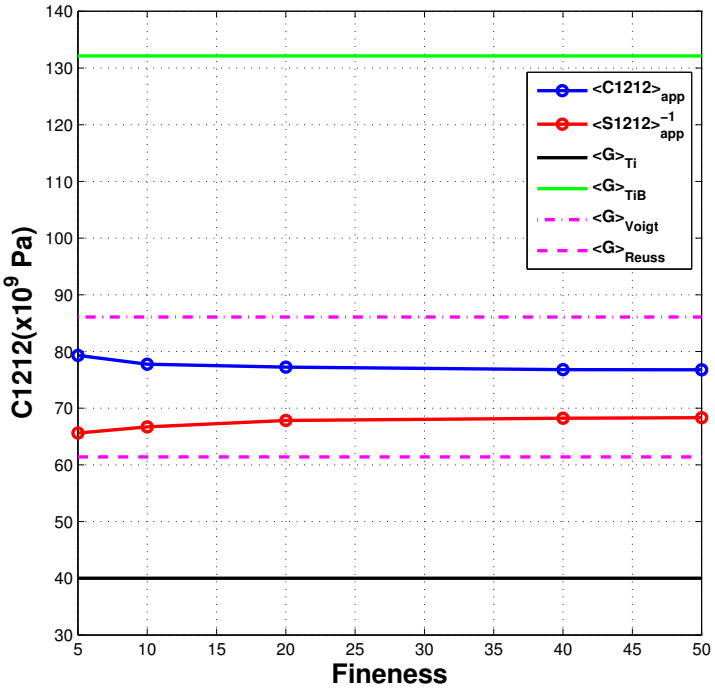

Figure 5.20: Shear response of a Ti-TiB graded microstructure in 3d

The green and black lines represent the shear moduli of the two phases (assuming local isotropic nature). The pink lines in Fig. 5.20 represent the classical Voigt (upper) and Reuss (lower) bounds calculated using equation (1.1) and (1.2) respectively. The shear responses of the graded microstructure under displacement (blue) and traction (red) boundary conditions are shown as well.

It can be observed from Fig. 5.20, that the bounds for the shear response converge too slow, and we fail to achieve RVE response as we increase our level of fineness. The difference in the shear response under the two boundary conditions is $\sim 21\%$ at fineness 5, and goes down to only $\sim 12\%$ at the largest analyzed fineness of 50. This is consistent with the results of the constitutive response of the graded microstructure in 2d (discussed in §5.3) where we fail to achieve a unique elastic-plastic constitutive response to the loading of the microstructure.

The results for the elastic homogenization of shear response for the Cu-Ni FGM are presented in Fig. 5.21.

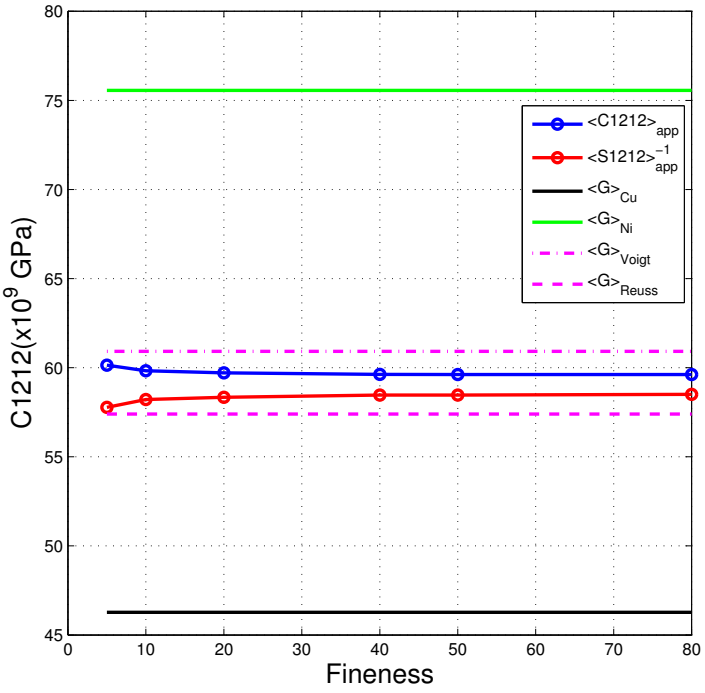

Figure 5.21: Shear response of a Cu-Ni graded microstructure in 3d

It can be observed from Fig. 5.21, that the bounds for the shear response converge faster than Ti-TiB, but we still fail to achieve the RVE response as we increase our level of fineness. The bounds converge faster due to the weaker contrast between the two material phases. The difference in the shear response under the two boundary conditions is $\sim 4\%$ at fineness 5, and goes down to only $\sim 2\%$ at the largest analyzed fineness of 80. This is consistent with the results of the constitutive response of the graded microstructure in 3d for Ti-TiB discussed earlier.

We now proceed to study the scaling function as described in §3.4. Due to the extremely expensive computational cost of the numerical simulations, we were able to numerically analyze the graded microstructures for only two phase contrasts.

Figure 5.22(a) corresponds to the scaling function (f) for the two FGM systems using equation (3.18). Figure 5.22(b) corresponds to the normalized scaling function (g) for the two FGM systems using equation (3.22).

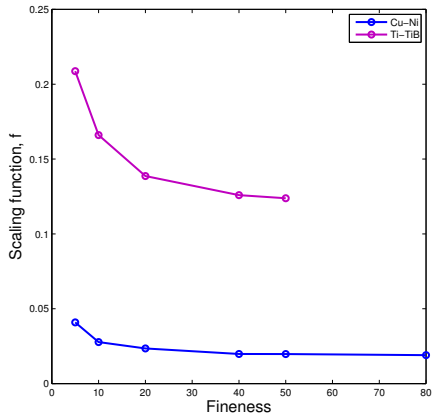

(a)

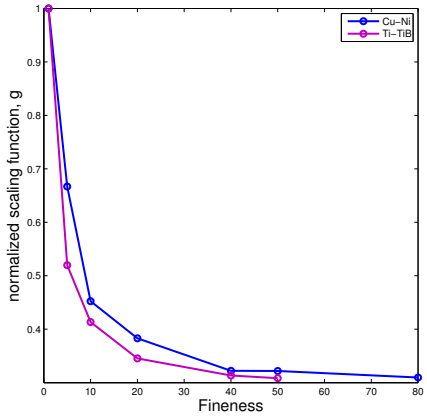

(b)

Figure 5.22: (a)Scaling function, f plotted against fineness (equation (3.18)), (b) Normalized scaling function, g plotted against fineness (equation (3.22))

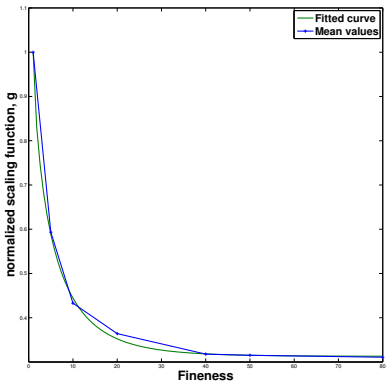

Figure 5.23: Normalized scaling function g, fitted with a stretch exponential function (green line)

On the basis of the mean values from Fig. 5.22(b), the normalized scaling function data was fitted using a *'stretched exponential'* function [47]. The effective normalized scaling function and it's fit are illustrated in Fig. 5.23. This fit of *'stretched exponential'* type takes the following form,

$$g(\delta) = 0.687exp[-0.331(\delta - 1)^{0.732}] + 0.313 \tag{5.12}$$

The scaling function and the fit thus obtained have been calculated using numerical data from only two contrasts for the graded microstructures. For more reliable data, we understand that we need to numerically simulate more contrasts at higher levels of finenesses (δ). The computational cost and the limitations on the current parallel computing clusters have thus far restricted us to the current level of simulations.

5.5 Fractal characterization of elastic-plastic transitions in 3d FGM

Due to the expensive nature of computational simulations in 3d, we have restricted ourselves to the elastic-plastic characterization of Ti-TiB graded microstructures in 3d (as discussed in §5.3). The material properties of the individual phases are tabulated in Table 5.1. The Ti grains in our simulations undergo plastic deformation according to equation (5.9). The TiB grains like earlier simulations in 2d remain elastic throughout our loading. Each of the material grains are assumed to be isotropic in nature and under perfect bonding.

The elastic-plastic simulations are more computationally intensive and expensive than elastic simulations (§2.3, §3.2, §5.4). Hence, to be able to effectively simulate large scales of fineness, we reduce our mesh density to 2, i.e. solving a realization of fineness 16 results in solving a problem of mesh $32 \times 32 \times 32$. The fineness scales under consideration were 8, 16, 32, and 50. Pure shear boundary conditions were applied using equations (5.10) and (5.11). The load applied (traction or displacements) on the graded microstructure are refined to a degree through which elastic-plastic transitions can be analyzed.

The simulations were carried out on *Blue Waters* currently housed at National Petascale Computing Facility at the NCSA. The nodes used at the facility were the XE compute nodes. Each of these nodes are equipped with two AMD 6276 Interlagos 2-core CPUs, and 16 cores total with 64GB of RAM. We used Abaqus/Standard 6.13 implicit direct parallel solver. The largest problem we could solve on this cluster was of fineness 50, i.e. problem of mesh $100 \times 100 \times 100$ over ten nodes taking approximately 12 hours.

5.5.1 Results

The results of the mechanical testing in 3d were plotted as volume averaged von Mises stress against a volume averaged plastic strain. This was done essentially to check the convergence of the constitutive response of the microstructure as we moved up our fineness scales.

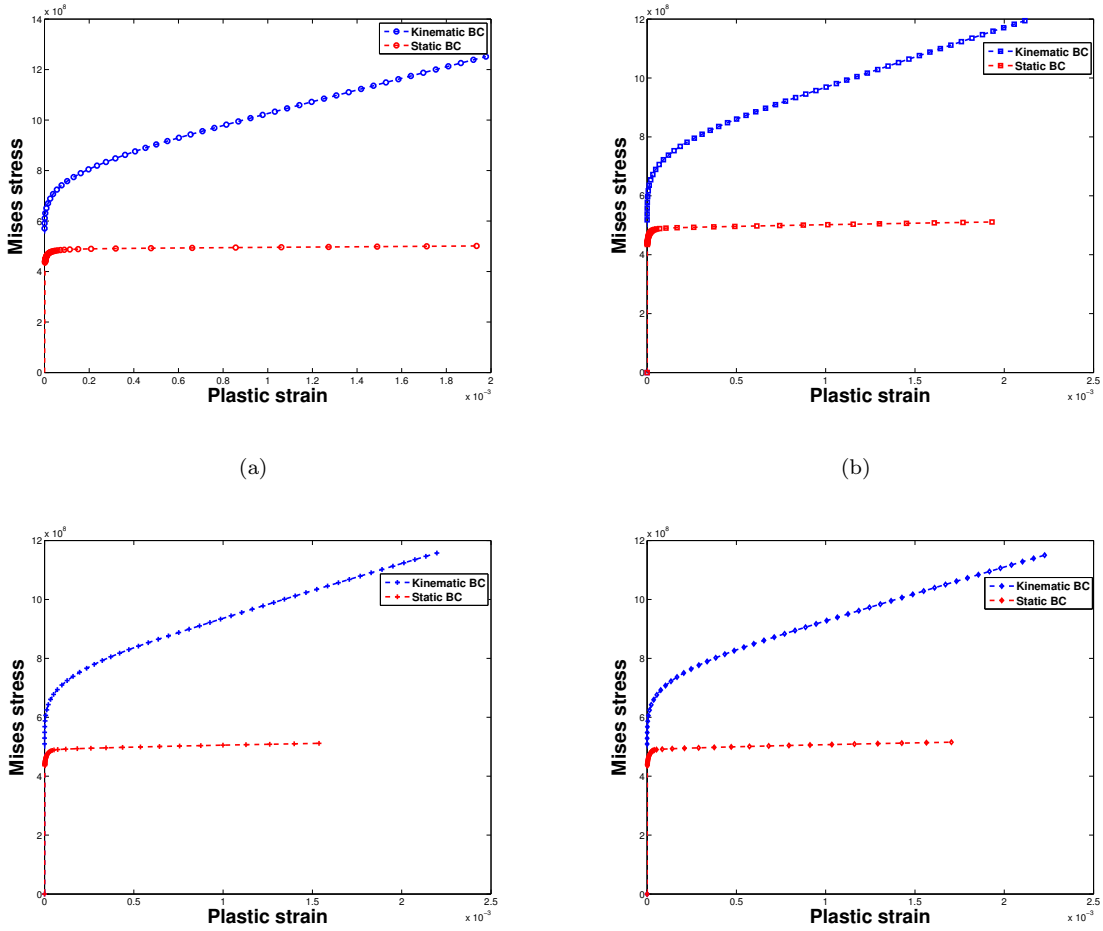

(a) (b)

(c) (d)

Figure 5.24: Elastic-plastic constitutive response at fineness (a) 8, (b) 16, (c) 32, (d) 50

Figure 5.24 shows the elasto-plastic constitutive response of the 3d graded microstructure at fineness from 8 to 50. To better observe the convergence as we increase our fineness, we overlay the plots from Fig. 5.24 onto Fig. 5.25. We can clearly observe from Fig. 5.25 that the RVE response is not achieved even after refining our fineness levels. This validates are findings in 2d graded microstructure where we also failed to uniquely characterize the constitutive response of the functionally graded material system.

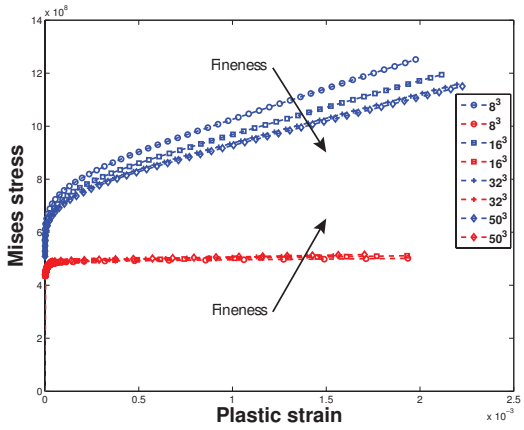

Figure 5.25: Combined stress strain plot for all fineness

To better understand the phenomenon taking place, we plot volume fraction of plastic grains against plastic strain for all levels of fineness under consideration.

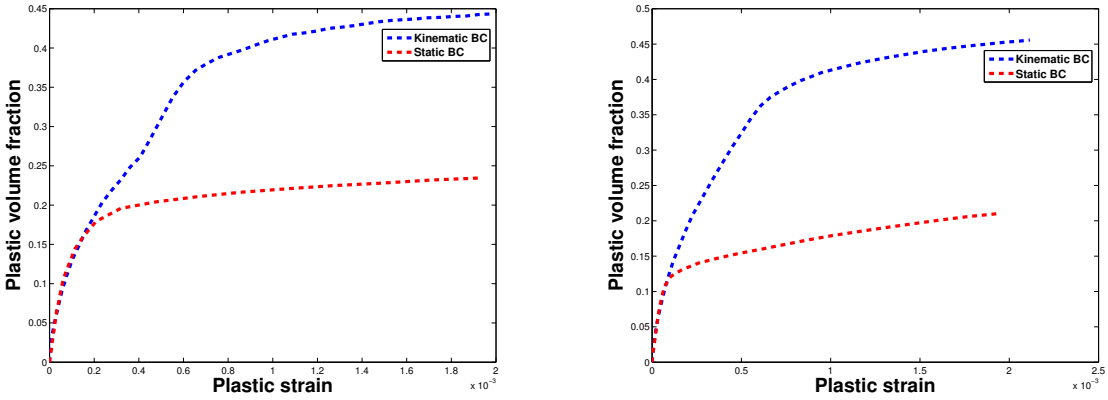

(a)

(b)

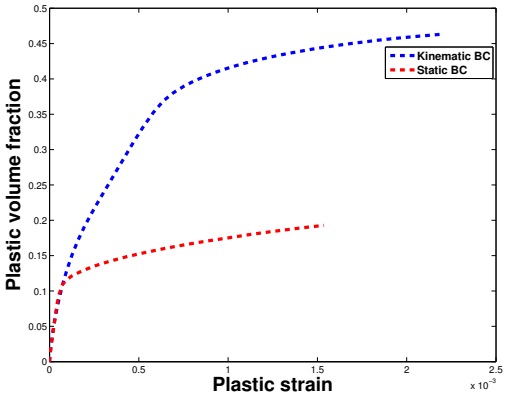

(c)

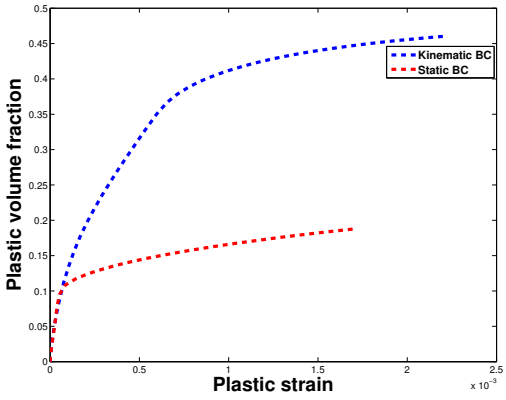

(d)

Figure 5.26: Evolution of plastic volume fraction in the graded microstructure at fineness (a) 8, (b) 16, (c) 32, (d) 50

It can be clearly seen from Fig. 5.26 that the evolution of plastic volume fraction in the graded microstructure is extremely sensitive to the loading conditions. Where under uniform kinematic boundary conditions we achieve plastic volume fraction of $\sim 45\%$ which suggests that almost all the Ti grains have gone plastic. Under static boundary conditions, we were able to achieve a plastic volume fraction of $\sim 20\%$. The evolution of plastic grains under both the boundary conditions in the microstructure at fineness 50 are shown below in Figs. 5.27 and 5.28. The transition from elastic state to plasticity is indicated by using the binary state in the sense that blue grains (elastic grains) turn to red grains (plastic grains) in Figs. 5.27 and 5.28 as we increase our load levels under both boundary conditions.

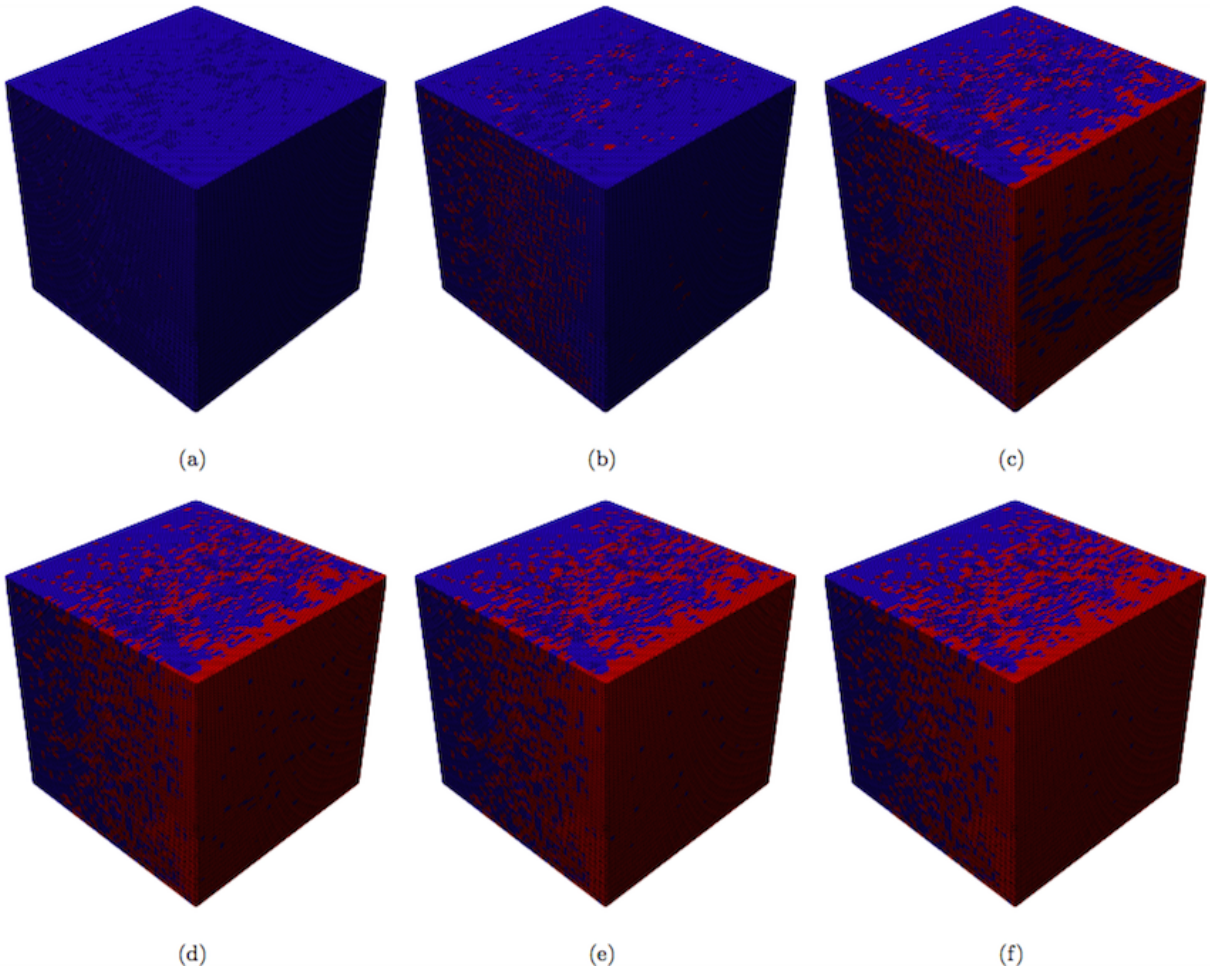

Figure 5.27: Evolution of plastic grains (red grains) in the microstructure at six different load levels under uniform kinematic boundary condition at fineness 50

As we can see from Fig. 5.27, the plastic grains are more uniformly distributed in the Ti domain. This is due to the fact that under displacement boundary conditions, the entire microstructure is subjected to uniform displacements. There is *'less'* localized plastic damage, as the plastic damage starts to accumulate in the middle where there is heavy interaction between Ti and TiB grains. The harder TiB grains press

against the softer Ti grains. As we increase our load, the plastic evolution spreads to Ti rich region. This plastic evolution is very different form the one observed under traction boundary condition (see Fig. 5.28).

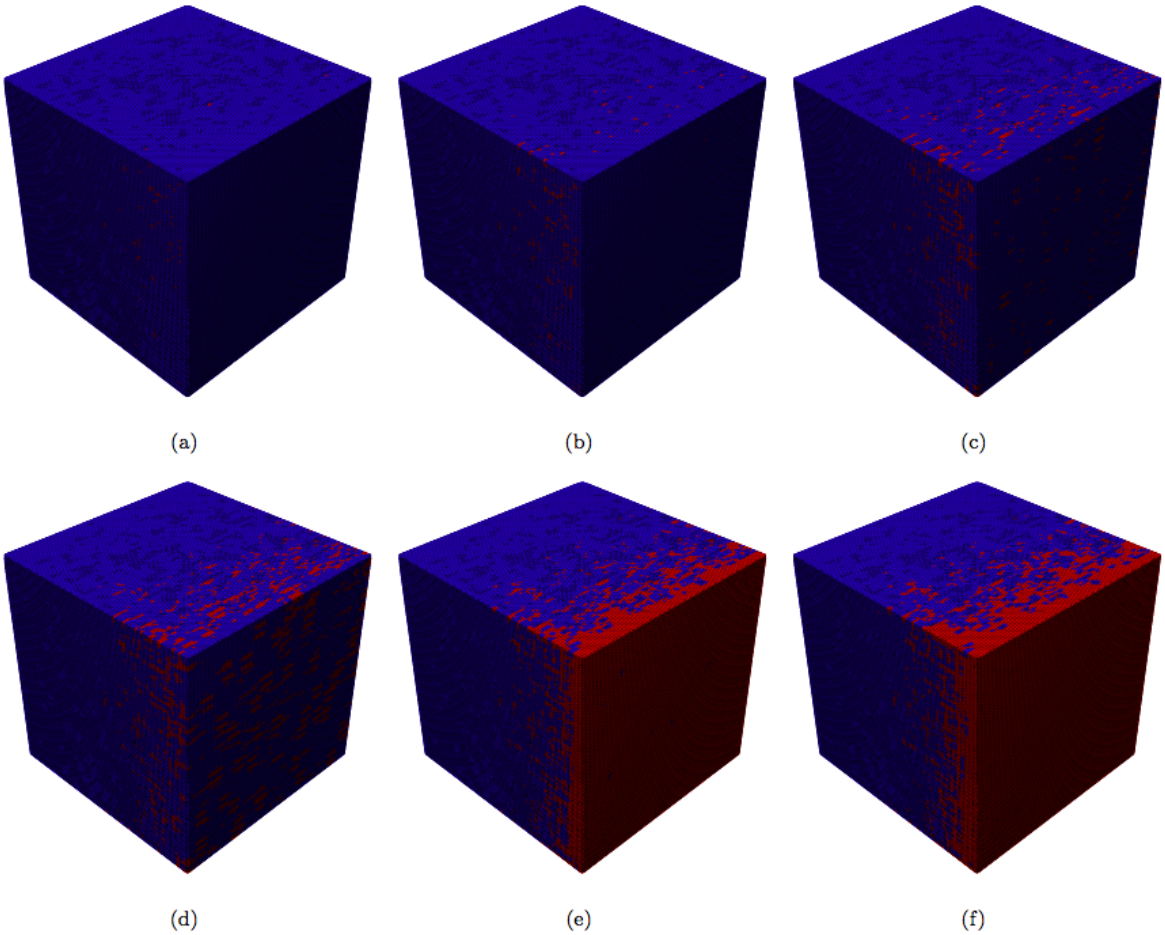

Figure 5.28: Evolution of plastic grains (red grains) in the microstructure at six different load levels under uniform static boundary condition at fineness 50

Figure 5.28 shows the evolution of plasticity under traction boundary condition. The evolution of plasticity starts in the Ti rich region, and as we increase our traction loads we see more of this evolution restricting itself to the Ti-rich region. This can be attributed to the fact that as we increase our loads the Ti grains in the Ti rich region start to undergo plastic deformation, and the plasticity becomes more localized in that region. The Ti grains in TiB rich region do not go plastic as the harder TiB grains have not been deformed as much as the Ti rich region resulting in very little deformation in that region.

We now measure the fractal dimension of the evolving plasticity in the microstructure under both the boundary conditions using the box-counting method as described in §4.2.1,

$$D = -\frac{log(N_r)}{log(r)} \tag{5.13}$$

Where, N_r denotes the number of boxes of size r to cover the plastic grains in the microstructure. The box sizes are chosen as a factor of our fineness 100, to avoid the partial covering of the plastic grains on the border. We verified our box-counting algorithm by measuring the fractal dimension of 3d cantor set. Our algorithm gives us the fractal dimension of 2.4852 against the exact theoretical fractal dimension of 2.4854. The $log(N_r) - log(r)$ plots corresponding to load levels in Figs. 5.27 and 5.28 are shown in Figs. 5.29 and 5.30 respectively.

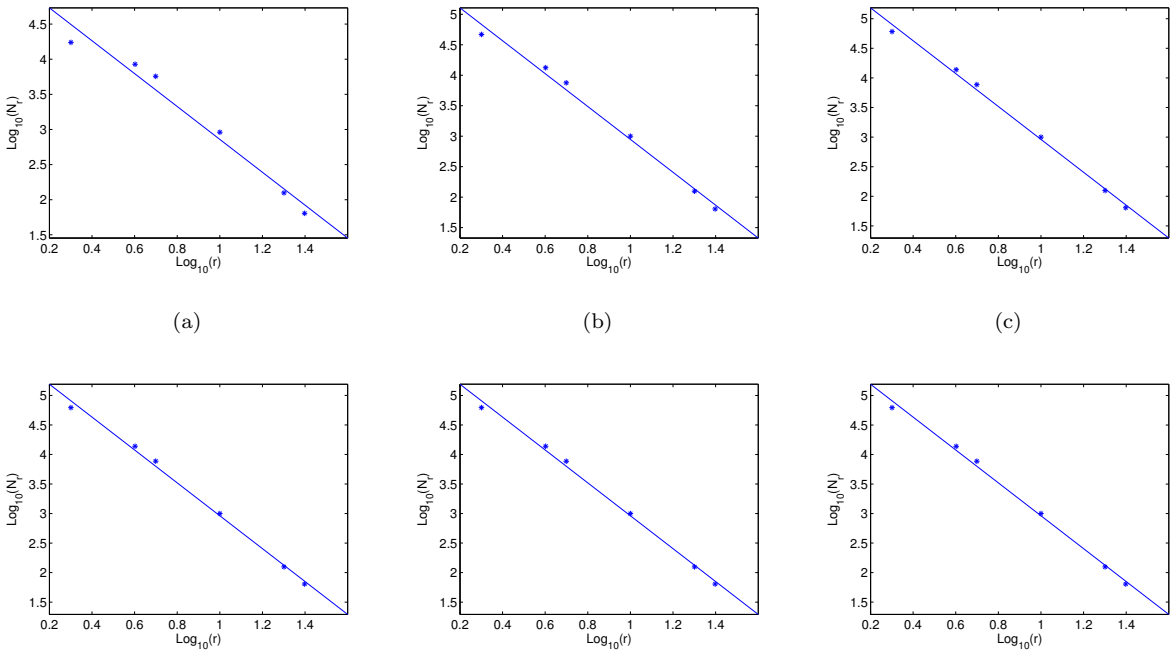

Figure 5.29: $log(N_r) - log(r)$ plots corresponding to load levels shown in Fig. 5.27 which are used to calculate fractal dimension using box-counting method

Figure 5.29 corresponds to displacement boundary condition, and Fig. 5.30 corresponds to traction boundary condition. The fractal dimensions and their correlation coefficients are listed in Tables 5.4 and 5.5 corresponding to displacement and traction boundary conditions respectively.

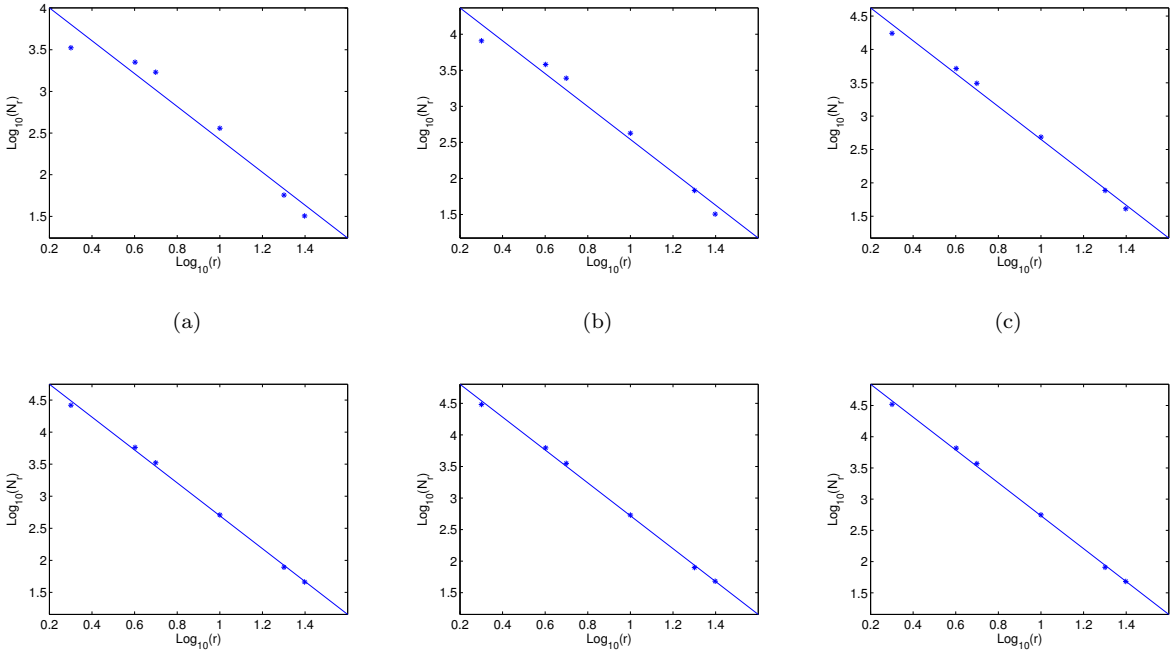

(a) (b) (c)

(d) (e) (f)

Figure 5.30: $log(N_r) - log(r)$ plots corresponding to load levels shown in Fig. 5.28 which are used to calculate fractal dimension using box-counting method

Field images	**Fractal dimension**	**Correlation coeffecient**
Figure 5.27(a)	2.3403	0.9852
Figure 5.27(b)	2.6980	0.9955
Figure 5.27(c)	2.7773	0.9977
Figure 5.27(d)	2.7837	0.9979
Figure 5.27(e)	2.7848	0.9979
Figure 5.27(f)	2.7852	0.9979

Table 5.4: Fractal dimension using box-counting method under displacement boundary condition

Field images	Fractal dimension	Correlation coeffecient
Figure 5.28(a)	1.9739	0.9748
Figure 5.28(b)	2.2804	0.9876
Figure 5.28(c)	2.4635	0.9965
Figure 5.28(d)	2.5648	0.9991
Figure 5.28(e)	2.6061	0.9993
Figure 5.28(f)	2.6335	0.9994

Table 5.5: Fractal dimension using box-counting method under traction boundary condition

For our box counting algorithm, the smallest possible box size ($r = 1$) is below are plastic grain spacing, while a large box size ($r = 50$) is too coarse to capture the fractal details of the evolving plastic grains. Since physical fractals are observed in finite geometrical scales, hence our box sizes our chosen from $r = 2 \rightarrow 25$. The correlation coefficients listed in Tables 5.4 and 5.5 are ~ 1, hence we conclude that the plastic evolution in our microstructure is fractal in nature.

Fractal dimension of fineness 32 are not reliable as it's too small a scale to estimate fractal dimension. Theoretically, our fineness scale should be as large as possible for reliable estimation of fractal dimension which is of fineness 50, i.e. mesh of 100^3 which is the largest fineness possible with the available computing resources.

We now plot the evolving fractal dimension against the evolving plastic volume fraction and plastic strain. This would allow us to see the evolution of fractal dimension against growing plasticity under both boundary conditions.

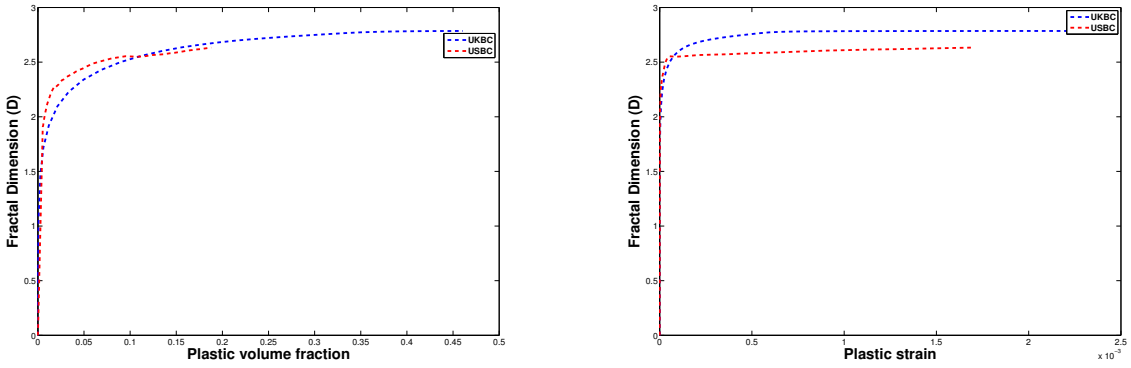

(a) (b)

Figure 5.31: Evolution of fractal dimension in fineness 50 against (a) Plastic volume fraction, (b) Plastic strain

As we can see from Fig. 5.31(a) that the fractal dimension of evolving plastic grains is different under both the boundary conditions, validating our earlier results in 2d that the FGM microstructure is extremely sensitive to the loading conditions. The localized plasticity under traction boundary condition gives us lower fractal dimension as compared to the the response under displacement boundary condition as can be seen from Fig. 5.31(b). Figure 5.31(b) also shows that fractal dimension can be a useful tool to measure the plastic strain the microstructure accumulates over it's loading history.

A. Saharan, S. Kale, S. Koric, L. Margetts and M. Ostoja-Starzewski, "Elastic-plastic transitions in three-dimensional randomly graded materials: Massively parallel simulations, fractal morphogenesis and scaling function," manuscript in preparation, 2014.

Chapter 6

Epilogue

6.1 Discussion

The classical bounds of Voigt-Reuss [56, 48] bounds and Hashin-Shtrikman [17] estimate the properties only as a function of volume fraction of the constituent phases. The microstructure's inherent randomness is lost in these methods which become extremely significant when estimating the properties below the RVE size. This dissertation studies the homogenization of various microstructures based on the Hill-Mandel macrohomogenity condition [19]. Thus the estimation of the effective properties is not only a function of volume fraction of the constituent phases, but also of the scale of observation.

In Chapter 2, we studied the simplest form of a random microstructure which is a two-phase random checkerboard. Our numerical analysis methodology was compared against microstructure independent analytical relations [31]. Our model converges asymptotically to the stated analytical expressions. After conforming to the analytical results, we proceeded to carry out our simulations for various constituent volume fraction at a higher contrast between the material properties of the constituent phases. We found that as we increased our scale of observation (mesoscale-δ), we converged to a constitutive RVE response of the microstructure. We also found that, for higher phase contrasts, the RVE response was achieved at a higher mesoscale.

In chapter 3, we turned our attention to two-phase correlated microstructures. The correlated microstructures under consideration were of Gaussian type. Scale dependent bounds in 2d on shear response are obtained for several contrasts in material properties of the phases. The effect of integral length scale λ, identified as the key microstructural length scale, and of the contrast (k), on the scale dependent bounds is analyzed through a systematic study based on the Hill-Mandel condition [19]. It is shown that increasing λ results in a slower convergence to the RVE. Interestingly, the scaling curves for different λ values can be simply collapsed after normalizing the mesoscale as δ/λ. Thus, the correlation length merely plays the role of a resolution scaling operator in a geometric sense even for the energy based bounds for Gaussian (short-range) correlations. A normalized scaling function $h(\delta/\lambda)$ of a power law form is observed to explain

the SVE-RVE transition over a wide parameter range of λ and k. In effect, the scaling function can be used in practice to determine the RVE size based on the microstructural correlation length scale λ and k of a two-phase material. In addition, our numerical model seems to be in agreement with experimental studies on correlated microstructures.

Chapter 4 introduces the concept of fractal dimension using box-counting method. The elastic-plastic transitions in a random homogeneous material are shown to be fractal in nature using box-counting method. This concept is then extended to analyze the elastic-plastic transition for non-homogenous microstructure like FGM in Chapter 5.

In Chapter 5 we look at microstructure of FGM type in 2d and 3d. The material system chosen in 2d was Titanium (Ti) - Titanium Monoboride (TiB), metal-ceramic functionally graded material system. The system has a piece-wise, one-dimensional geometry. Various fineness scales have been considered for both geometrical interpretation and mechanical testing through the finite element analysis.

Edge sets (interfaces between the black and white interfaces) were plotted for various fineness and found them sparse near the boundaries and dense in the middle for each of our simulations. We then measured the interfacial fractal dimension, and observed a high noise in it for lower fineness levels. Also, there is no trend seen in the variation of fractal dimension locally as we move widthwise (but not top-to-bottom). However, we see a clear trend moving lengthwise (left to right), which, in fact, can be characterized by a complicated relation given by a Fourier fit. A simple relation involving the Beta function can also be used to characterize the same, with both relations having comparable residuals.

Mechanical testing was carried out using the commercial FEA package, ABAQUS. Titanium grains in the FGM were assumed to be isotropic elastically with isotropic plastic hardening. TiB grains in the FGM were assumed to be elastically isotropic throughout. By using both the UKBC (displacement BC) and USBC (traction BC), we applied pure shear loading on our model; it was observed that our model did not result in a classical constitutive RVE response. This means that the homogenization based on the Hill condition is extremely sensitive to the loading conditions. The plastic evolution of the Titanium grains under both boundary conditions displayed a fractal plane-filling behavior. The plastic grains under UKBC started evolving from the TiB rich region (containing some Titanium Grains) and spread towards the Titanium rich region progressing rather uniformly. Under USBC the plastic grains evolved mainly from the Titanium rich region and remained concentrated mainly in the same region. This fractal behavior was measured for both loading conditions using the box counting method. However, the fractal dimension under UKBC and USBC had different values. This validates our earlier result that the model response is highly sensitive to the loading conditions.

We then extended our study to FGMs in 3d. Two material systems, Ti-TiB and Copper (Cu) - Nickel (Ni). We performed the elastic homogenization of the shear response, and found that like in elastic-plastic analysis in 2d, the elastic shear response also fails to homogenize at higher levels of fineness. The bounds from both boundary conditions fail to converge, and the gap between the responses depends on the contrast in the material properties of the phases present. For weak contrast (Cu-Ni), we found the gap between the bounds lower than that for higher contrast (Ti-TiB).

The elastic-plastic transitions for 3d FGM (Ti-TiB) were also found to be fractal in nature. The constitutive response was observed to be sensitive to the loading conditions. The fractal dimension calculated of the evolving plastic grains was different under both displacement and traction boundary conditions validating our mechanical results. Overall, the results obtained for 3d FGM microstructure were well in agreement with the results obtained for 2d FGM microstructure obtained in §5.3.

6.2 Concluding remarks

- Uncorrelated random microstructures (Chapter 2), and correlated random microstructures (Chapter 3) are successfully homogenized using the Hill-Mandel macrohomogenity condition.
- Scale dependent bounds using the Hill-Mandel macrohomogenity condition offers a better estimation of the RVE properties than classical bounds at different volume fractions.
- The higher contrast between the constituent phases yields in a larger RVE size
- The correlation length (λ) inversely effects the convergence of bounds in correlated microstructure.
- The proposed scaling function proposed can be used to predict the RVE size of any correlated microstructure for a range of phase contrasts (k) and correlation length (λ).
- Elastic homogenization of FGM microstructure fails due to a non-unique constitutive response.
- The elastic-plastic constitutive response of the FGM fails to homogenize suggesting the material model is extremely sensitive to the loading conditions.
- The evolution of plasticity in FGM is smooth in terms of the stress-strain curve and the spatial patterns of elastic-plastic transitions are fractal.
- The fractal dimension of the evolving plastic sets in the material under both boundary conditions (kinematic or traction) also shows a difference, validating our conclusion that the constitutive response of the material in not unique.

6.3 Future Opportunities

The present work can be extended to many future opportunities. Our technique can be used to extend the study on correlated microstructures to obtain bounds on bulk moduli in 2d to completely describe the constitutive response. The same can also be extended to correlated microstructures in 3d, and various physical phenomenon like thermal and electrical conductivity can be studied. Studies could also be conducted for anisotropic Gaussian correlated microstructures (where $\gamma_1 \neq \gamma_2$, see equation (3.3)).

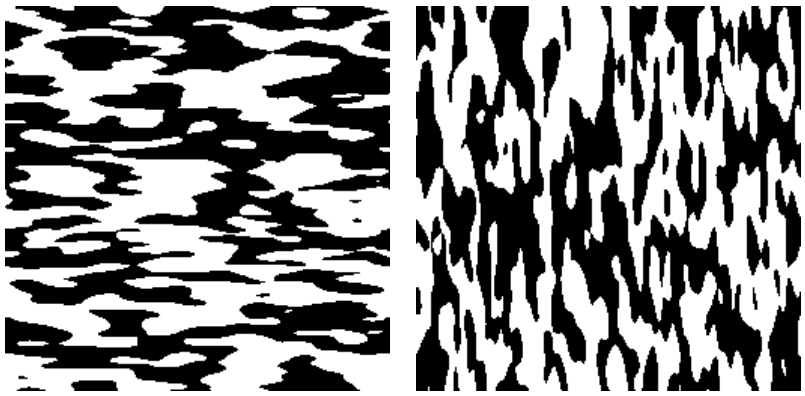

(a) (b)

Figure 6.1: Anisotropic correlated Gaussian microstructures generated using algorithm given by Makse *et al.* [28] (see appendix A)

This research also opens up the possibility to analyze the behavior of long range correlated microstructures in an attempt to better understand the behavior at scales not explored as yet.

The fractal geometry interpretation presented in this study can be used to study the behavior of FGMs where the mismatch in properties across the interfaces of two phases are important - for example the heat transfer, electrical or magnetic conductivity, etc. The mechanical results show that the fractal dimension can be used to estimate the plasticity in a material for damage assessment in various mechanical equipment, presenting a good alternative to expensive strain gages, which require considerable amount of effort to install.

The scaling laws studied for FGMs in §5.4.2 need to be formulated by studying a comprehensive set of material systems. The FGM microstructure is not isotropic in nature, hence homogenization of the entire stiffness matrix is essential to understand their behavior completely. Since, due to limitations of the commercially available software ABAQUS on parallel computing architecture, a more robust FEA tool is required to perform these analysis in parallel efficiently. One option is to use an open source code called *'ParaFEM'* [54]. This code has been built by Dr. Lee Margetts from University of Manchester, UK. Currently a collaboration is in the works with Dr. Lee Margetts to use their FEA code for our complex

microstructure simulations.

Further there is a need to experimentally validate our results obtained for elastic homogenization, and elastic-plastic constitutive response for 3d FGMs. A preliminary experimental study was conducted using samples made by additive manufacturing technology (see §6.3.1).

6.3.1 Experimental study

An preliminary experimental study was carried out in an effort to validate our elastic homogenization results obtained in §5.4.2. The samples were prepared using additive manufacturing technology. As a first step, we wrote computer code to write *'STL file format'* (STereoLithography) for our FGM microstructure. This file format is essential for the 3d printers to read and print accordingly.

The 3d printing facility utilized was located at the Rapid Prototyping Laboratory in Mechanical Engineering Laboratory (MEL) at University of Illinois Urbana-Champaign (UIUC). The equipment used to make our samples was OBJET Eden 350 3-Dimensional Printing System (see figure 6.2).

Figure 6.2: OBJET Eden 350 3d printer located at MEL, UIUC

One of the samples produced by the 3d printer are shown in figure 6.3.

Figure 6.3: A 3d printed FGM sample

As can be clearly seen from figure 6.3, we have a sample with blue phase on the right which slowly grades

into white phase on the left giving us a graded microstructure.

The blue material in the sample is $VeroBlueFullCure^{®}840$ and the white phase is $SupportFullCure^{®}705$. The material properties of $VeroBlueFullCure^{®}840$ are given in Table 6.1. The $SupportFullCure^{®}705$ material is a soft *'gel'* like material which is used by the 3d printer to support the model material ($VeroBlueFullCure^{®}840$) as it prints the samples layer by layer. The material properties of this support material are unknown, and mechanical testing may be required to determine it's mechanical properties.

Property	**ASTM**	**Value**	**Metric**
Tensile Strength	D-638-03	55	MPa
Modulus of Elasticity	D-638-04	2740	MPa

Table 6.1: Material properties of VeroBlue material

Uniaxial tensile test was carried out using these samples on DMA (Dynamic Mechanical Analysis) Q800 instrument (shown in figure 6.4) located at Frederick Seitz Materials Research Laboratory Central Research Facilities, University of Illinois.

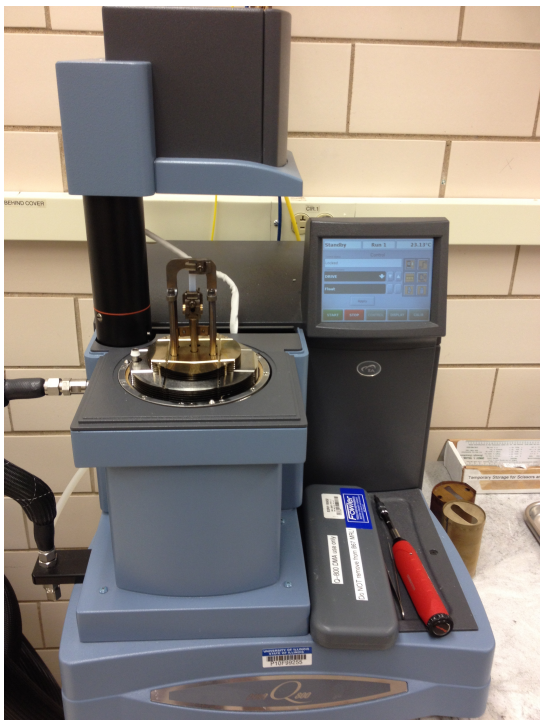

Figure 6.4: DMA Q800 instrument

The specimen dimensions for the tensile test on these instruments were $5 - 30mm \times 8mm \times 2mm$. The samples were printed in *'Matte'* finish, i.e. the entire sample was surrounded by the support material. The

samples were then cut carefully to the given dimensions using a razor blade. The mean dimensions for the samples were $19.35 \pm 3.24mm \times 6.35 \pm 0.15mm \times 2.37 \pm 0.23mm$.

The instrument fixture with our FGM sample being clamped in it is shown in figure 6.5.

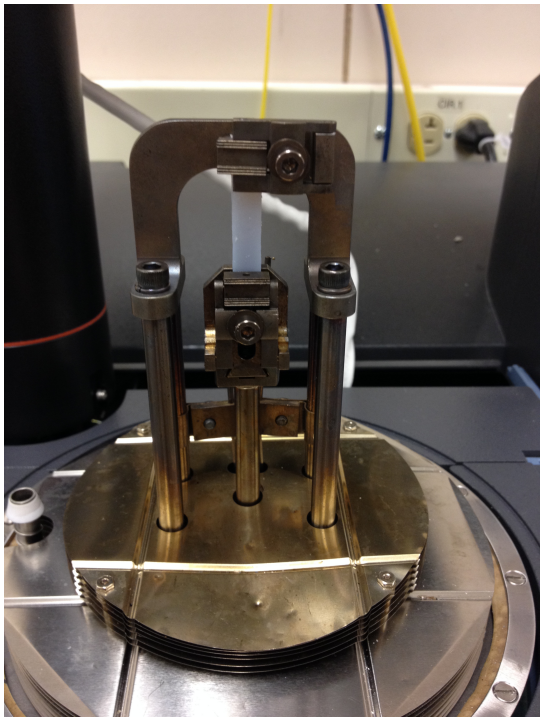

Figure 6.5: FGM sample clamped in DMA Q800 before loading

The experiment performed was a uniaxial tensile test under *'force control'* loading conditions. The experimental parameters are listed below,

- Pre-load of 0.0001 N was applied. This was the minimum pre-load that can be applied using the DMA Q800. The pre-load was applied to measure the length of the specimens in between the clamps.
- The loading rate for the experiments was $0.05N/min$. The upper limit for the applied load was set at $5N$.
- The torque applied to hold the specimen in clamps was $0.2in - lb(0.0023m - Kg)$. Since the support material is very soft, hence any more torque to tighten the clamps resulted in disintegration of the sample from the soft side. The printed samples were really *'slippery'* on the clamps at such low torques, hence this was a trade-off.
- All the experiments were performed at room temperature.

The constitutive response of the various samples tested are presented in figure 6.6. The constitutive response of the 3d printed FGM samples show a wide scatter. The samples exhibit non-linear elastic behavior which suggests that the samples are viscoelastic in nature to a large degree, and hence cannot be modeled by classical linear elastic models. The viscoelastic nature of the samples also can be attributed to the wide scatter, as viscoelastic materials are known to exhibit a wide scatter in constitutive behavior.

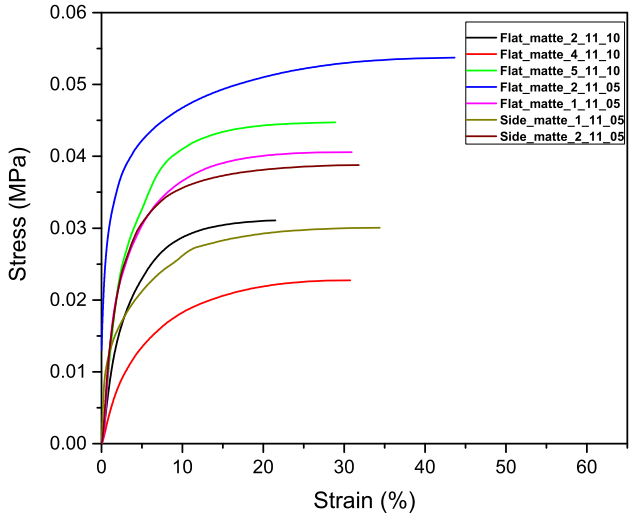

(a)

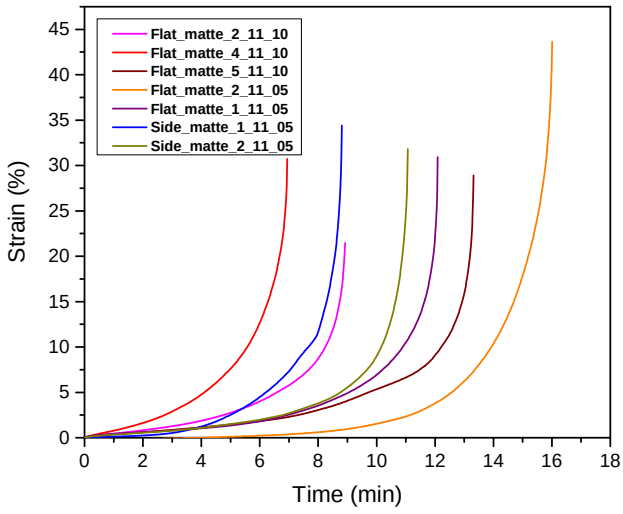

(b)

Figure 6.6: (a) Stress-strain plots for 3d printed FGM samples, (b) Strain-time plots for 3d printed FGM samples

Due to the *'slippery'* nature of the sample surface, most of the samples slipped out of the clamps at the end of the load step. So, the slope after the yield can be attributed to various factors such as slipping, internal fatigue which needs to be investigated further.

To demonstrate the viscoelastic nature of the samples we performed stress-relaxation test (see figure 6.7) on our 3d printed samples. A constant displacement of $\sim 13.2\mu m$ was applied to our samples. As can be observed from figure 6.7, the samples relieve considerable amount of stress under constant strain showing the viscoelastic nature of the materials.

A creep test could also be investigated for these samples, and a similar model based on Hill-Mandel macrohomogenization condition for viscoelastic materials can be built. The numerical results from that model can be validated by the experimental data presented here.

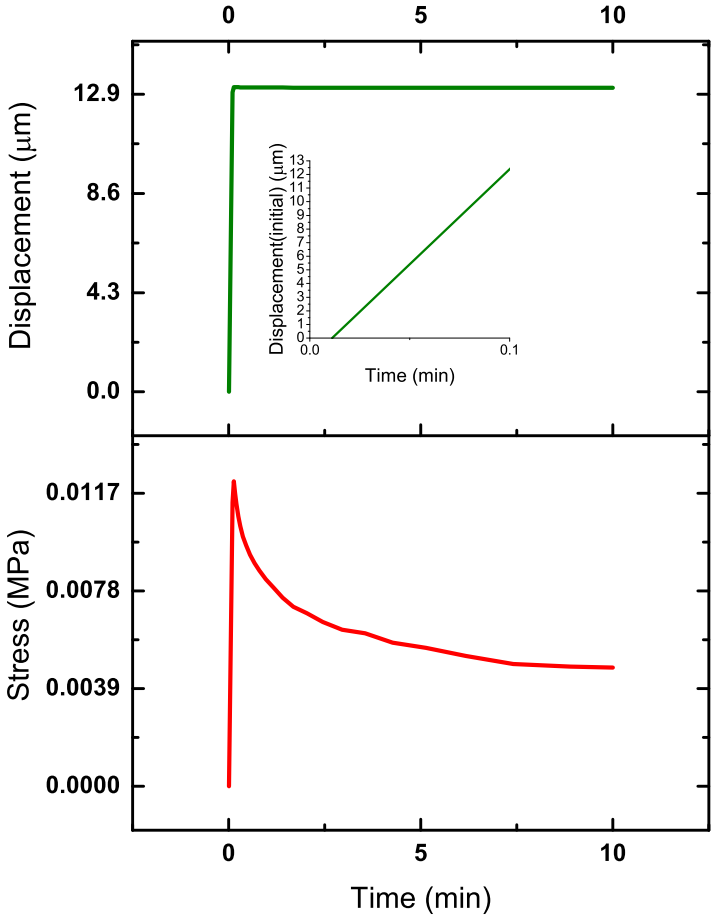

Figure 6.7: Stress relaxation test on 3d printed FGM samples

Appendix A

Generation of Gaussian correlated microstructures

In this section we outline the steps involved in generating the Gaussian correlated microstructures used in this study. The correlated microstructures are generated by thresholding the random numbers having the desired spatial correlations over a 2d domain of size δ. The correlated random numbers are generated using the Fourier Filtering Method (FFM) as follows,

1. Random numbers $\eta_r \in [0, 1]$ are generated on a grid of size $\delta \times \delta$.

2. The spectral density $S(q_x, q_y)$ of the Gaussian correlation function $\rho(x, y)$ given in equation (3.3) is calculated analytically as

$$S(q_x, q_y) = \frac{\exp\left[-\frac{1}{4}\left(\frac{q_x^2}{\gamma_1} + \frac{q_y^2}{\gamma_2}\right)\right]}{\sqrt{4\gamma_1\gamma_2}} \tag{A.1}$$

   where, q_x and q_y are the wavenumbers along x and y, respectively. For the isotropic case considered in this study, the coefficients $\gamma_1 = \gamma_2 = \gamma$ are related to λ as given in equation (3.6).

3. Obtain the Fourier transform coefficients s_i using

$$s_i = s_r\sqrt{S(q_x, q_y)} \tag{A.2}$$

   where s_r are the Fourier transform coefficients of η_r. s_i are the Fourier transform coefficients of the desired set of Gaussian correlated random numbers η_i.

4. Take the inverse Fourier transform of s_i to obtain η_i on a $\delta \times \delta$ grid.

The Gaussian correlated random numbers $\eta_i \in [-0.5, 0.5]$ generated using these steps for $\lambda = 1, 4$ and 16 on a mesodomain of size $\delta = 256$ are shown in figure A.1(a)-A.1(c), respectively.

To generate the two-phase microstructure from the correlated random numbers, we need to specify a threshold η_{th} such that all points in the domain with $\eta_i > \eta_{\text{th}}$ belongs to the white phase and the rest

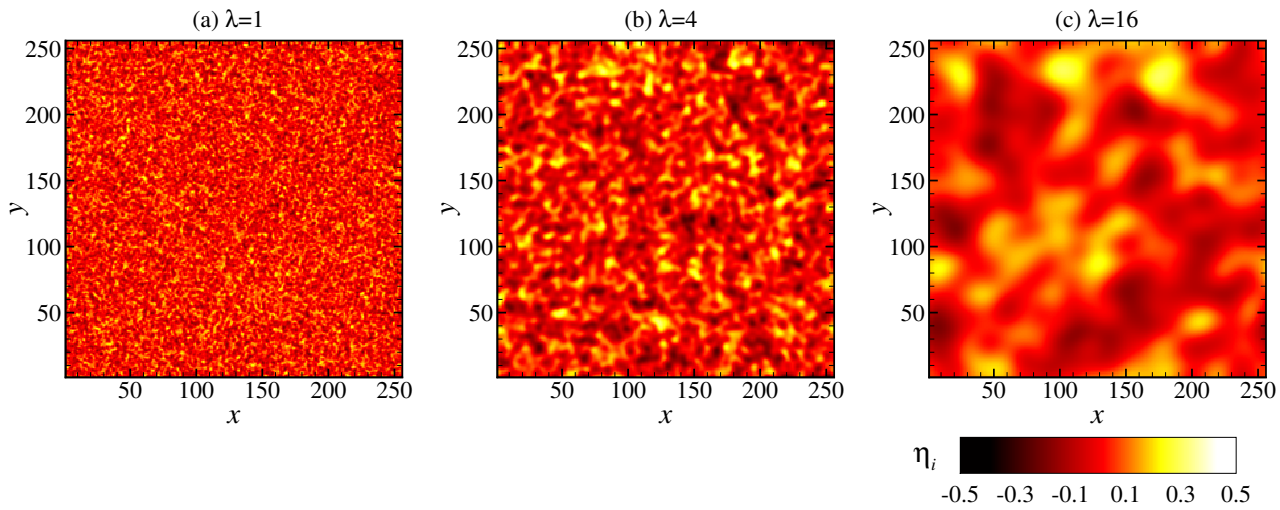

Figure A.1: The Gaussian correlated random numbers generated by the FFT based method described in Appendix A for (a) $\lambda = 1$, (b) $\lambda = 4$ and (c) $\lambda = 16$ on a mesoscale size of $\delta = 256$. The two-phase microstructure is extracted by imposing a threshold between -0.5 and 0.5 such that the η_i values above the threshold belong to the white phase and the remaining to the black phase. The value of the threshold is chosen to get the desired volume fractions.

belongs to the black phase. The value of η_{th} is chosen such that the actual volume fraction of the phases is the closest to the desired volume fraction.

References

[1] J. Aboudi, M.J. Pindera, and S.M. Arnold. Thermoplasticity theory for bidirectionally functionally graded materials. *J. Therm. Stresses*, 19(9):809–861, 1996.

[2] D.E. Aldrich, Z. Fan, and P. Mummery. Processing, microstructure, and physical properties of interpenetrating al2o3/ni composites. *Materials Science and Technology*, 16(7-8):747–752, 2000. cited By (since 1996)11.

[3] Ganesh Anandakumar, Na Li, Atul Verma, Prabhakar Singh, and Jeong-Ho Kim. Thermal stress and probability of failure analyses of functionally graded solid oxide fuel cells. *J. Power Sources*, 195(19):6659 – 6670, 2010.

[4] A.S. Balankin. Probabilisitc mechanics self-affine cracks in paper sheets. *Eng. Fract. Mech.*, 57:135–203, 1997.

[5] A.S. Balankin, L.H. Hernandez, G. Urriolagoitia, O. Susarrey, J.M. González, and J. Martinez. Probabilisitc mechanics of self-affine cracks in paper sheets. *Proc. R. Soc. Lond.*, A 455:2565–2575, 1999.

[6] M.F. Barnsley. *Fractals Everywhere*. 1993.

[7] F.M. Borodich. Fractals and fractal scaling in fracture mechanics. *Int. J. Fract.*, 95:239–259, 1999.

[8] R. Boyer, W. Gerhard, and E.W. Collings. *Material properties handbook: Titanium Alloys*. ASM International, 1994.

[9] Bernard Budiansky and T. T. Wu. Theoretical prediction of plastic strains of polycrystals. Technical report, DTIC Document, 1961.

[10] C-FIT. *C-FIT User Guide*. Center for Engineering Research Inc.

[11] B.P. Chandi. *Strain hardening of titanium by severe plastic deformation*. PhD thesis, Massachusetts Institute of Technology, Cambridge, Massachusetts, 1973.

[12] Ahmed Saleh Dalaq, Shivakumar I. Ranganathan, and Martin Ostoja-Starzewski. Scaling function in conductivity of planar random checkerboards. *Comp. Mater. Sci.*, 79(0):252 – 261, 2013.

[13] K.A. de Campos, Y. Celso, and Luis Rogerio de Oliveira Hein. Fractal behavior throughout stretch zone of 15-5ph steel under elastic-plastic loading conditions. *Mater. Sci. Eng.*, A 525:37–41, 2009.

[14] X Du and M Ostoja-Starzewski. On the size of representative volume element for darcy law in random media. *Proc. Roy. Soc. A.*, 462(2074):2949–2963, 2006.

[15] J. D. Eshelby. The determination of the elastic field of an ellipsoidal inclusion, and related problems. *Proc. Roy. Soc. Lond. A.*, 241(1226):376–396, 1957.

[16] Recep Gunes and Murat Aydin. Elastic response of functionally graded circular plates under a drop-weight. *Compos. Struct.*, 92(10):2445 – 2456, 2010.

[17] Z. Hashin and S. Shtrikman. A variational approach to the theory of the elastic beaviour of multiphase materials. *J. Mech. Phys. Solids*, 11:127–140, 1963.

[18] H.J. Herrmann, A.N.B Poliakov, and F. Tzschichholz. The deformation of rocks: Fractals everywhere. *Fractals*, 3(4):821–828, 1995.

[19] R. Hill. Elastic properties of reinforced solids: Some theoretical principles. *J. Mech. Phys. Solids*, 11(5):357 – 372, 1963.

[20] Seyed Mahmoud Hosseini and Farzad Shahabian. Reliability of stress field in al2o3 functionally graded thick hollow cylinder subjected to sudden unloading, considering uncertain mechanical properties. *Mater. Design*, 31(8):3748 – 3760, 2010.

[21] Yang Jiao, Eric Padilla, and Nikhilesh Chawla. Modeling and predicting microstructure evolution in lead/tin alloy via correlation functions and stochastic material reconstruction. *Acta Mater.*, 61(9):3370 – 3377, 2013.

[22] T. Kanit, S. Forest, I. Galliet, V. Mounoury, and D. Jeulin. Determination of the size of the representative volume element for random composites: statistical and numerical approach. *Int. J. Solids Struct.*, 40(1314):3647 – 3679, 2003.

[23] Ekkehart Kröner. Berechnung der elastischen konstanten des vielkristalls aus den konstanten des einkristalls. *Zeitschrift fr Physik*, 151(4):504–518, 1958.

[24] Reid A. Larson. *A Novel Method For Characterizing the Impact A Novel Method For Characterizing the Impact A Novel Method For Characterizing the Impact A novel method for characterizing the impact response of functionally graded plates*. PhD thesis, Air Force Institute of Technology, Wright-Patterson Air Force Base, Ohio, September 2008.

[25] J. Li and M. Ostoja-Starzewski. Fractal pattern formation at elastic-plastic transition in heterogeneous materials. *ASME J. Appl. Mech*, 77, 2010.

[26] J. Li and M. Ostoja-Starzewski. Fractals in elastic-hardening plastic materials. *Proc. R. Soc. Lond.*, A 466:603–621, 2010.

[27] J. Li, A. Saharan, S. Koric, and M. Ostoja-Starzewski. Elastic-plastic transition in three-dimensional random materials: massively parallel simulations, fractal morphogenesis and scaling functions. *Phil. Mag.*, 92(22):2733 – 2758, 2012.

[28] H.A. Makse, S. Havlin, M. Schwartz, and H.E. Stanley. Method for generating long-range correlations for large systems. *Phys. Rev. E*, 53(5 SUPPL. B):5445–5449, 1996. cited By (since 1996)221.

[29] B. Mandelbrot. *The Fractal Geometry of Nature*. 1982.

[30] Mandelbrot.B. How long is coast of Britain - statistical self-similarity and fractional dimension. *SCIENCE*, 156(3775):636–&, 1967.

[31] G.W. Milton. *The theory of composites*. Cambridge University Press, 2004.

[32] Y. Miyamoto, W.A. Kaysser, B.H. Rabin, A. Kawasaki, and R.G. Ford. *Functionally Graded Materials: Design, Processing and Applications*. Kluwer Academic Publishers, 1999.

[33] T Mori and K Tanaka. Average stress in matrix and average elastic energy of materials with misfitting inclusions. *Acta. Metall. Mater.*, 21(5):571 – 574, 1973.

[34] J. Li M. Ostoja-Starzewski. Fractals in thermo-elasto-plastic materials. *J. Mech. Mater. Struct. (C.R. and M.-L. Steele special issue)*, 6(1-4):351–359, 2011.

[35] M. Ostoja-Starzewski. Micromechanics model of ice fields - ii: Monte carlo simulation. *Pure Appl. Geoph*, 133(2):229–249, 1990.

[36] M. Ostoja-Starzewski. *Microstructural randomness and scaling in mechanics of materials*. Chapman and Hall/CRC, Boca Raton, Florida, 2008.

[37] M. Ostoja-Starzewski and J. Schulte. Bounding of effective thermal conductivities of multiscale materials by essential and natural boundary conditions. *Phys. Rev. B*, 54:278–285, Jul 1996.

[38] K.B. Panda and K.S. Ravi Chandran. Titanium-titanium boride (ti-tib) functionally graded materials through reaction sintering: Synthesis, microstructure, and properties. *Metall. Mater. Trans. A*, 34(9):1993–2003, 2003.

[39] Kyoungsoo Park and Glaucio H Paulino. Parallel computing of wave propagation in three dimensional functionally graded media. *Mech. Res. Commun.*, 38(6):431–436, 2011.

[40] Glaucio H Paulino and Alok Sutradhar. A simple Galerkin boundary element method for three-dimensional crack problems in functionally graded materials. In *Materials Science Forum*, volume 492, pages 367–372. Trans Tech Publ, 2005.

[41] Glaucio H Paulino and Alok Sutradhar. The simple boundary element method for multiple cracks in functionally graded media governed by potential theory: a three-dimensional Galerkin approach. *Int. J. Numer. Meth. Eng.*, 65(12):2007–2034, 2006.

[42] A.N.B Poliakov, H.J. Herrmann, Y.Y. Podladchikov, and S. Roux. Fractal plastic shear bands. *Fractals*, 2(4):567–581, 1994.

[43] Prokofiev. Fractal dimension: Covering of a fractal curve (here the coast of great britain) by grids of decreasing sizes. to measure the box-counting dimension, we count how many squares contain parts of the curve. @ONLINE, 2010.

[44] BharathV. Raghavan and ShivakumarI. Ranganathan. Bounds and scaling laws at finite scales in planar elasticity. *Acta Mech.*, pages 1–16, 2014.

[45] Shivakumar I. Ranganathan and Martin Ostoja-Starzewski. Mesoscale conductivity and scaling function in aggregates of cubic, trigonal, hexagonal, and tetragonal crystals. *Phys. Rev. B*, 77:214308, Jun 2008.

[46] Shivakumar I. Ranganathan and Martin Ostoja-Starzewski. Scale-dependent homogenization of inelastic random polycrystals. *J. Appl. Mech.-T. ASME*, 75(5), SEP 2008.

[47] Shivakumar I Ranganathan and Martin Ostoja-Starzewski. Scaling function, anisotropy and the size of rve in elastic random polycrystals. *J. Mech. Phys. Solids*, 56(9):2773–2791, 2008.

[48] A. Reuss. Berechnung der fließgrenze von mischkristallen auf grund der plastizitätsbedingung für einkristalle. *J. Appl. Math. Mech.*, 9:49–58, 1929.

[49] Wilfredo Montealegre Rubio, Glaucio H Paulino, and Emilio Carlos Nelli Silva. Analysis, manufacture and characterization of ni/cu functionally graded structures. *Mater. Design*, 41:255–265, 2012.

[50] A. Saharan, M. Ostoja-Starzewski, and S. Koric. Fractal geometric characterization of functionally graded materials. *J. Nanomech. and Micromech.*, 3(4):04013001, 2013.

[51] Ankit Saharan. Characterization of functionally graded materials through fractal geometry. Master's thesis, University of Illinois at Urbana-Champaign, USA, 2010.

[52] Takashi Saito. The automotive application of discontinuously reinforced tib-ti composites. *JOM*, 56(5):33–36, 2004.

[53] EmílioCarlosNelli Silva, MatthewC. Walters, and GlaucioH. Paulino. Modeling bamboo as a functionally graded material: lessons for the analysis of affordable materials. *J. Mater. Sci.*, 41(21):6991–7004, 2006.

[54] I.M. Smith, D.V. Griffiths, and L. Margetts. *Programming the Finite Element Method*. John Wiley & Sons Ltd., The Atrium, Southern Gate, Chichester, West Sussex, U.K., 2013.

[55] Senthil S. Vel and Andrew J. Goupee. Multiscale thermoelastic analysis of random heterogeneous materials: Part i: Microstructure characterization and homogenization of material properties. *Comp. Mater. Sci.*, 48(1):22 – 38, 2010.

[56] W. Voigt. Theoretische Studien über die Elasticitätsverhältnisse der Krystalle. *Abh.Kgl.Ges.Wiss.Göttingen, Math.Kl*, 34:3–51, 1887.